Mathematical modelling of fungi-initiated siderophore-iron interactions

M. Jabed A. Choudhury, Philip M. J. Trevelyan & Graeme P. Boswell*
Dept. of Mathematics and Statistics, University of South Wales,
Pontypridd, CF37 1DL, UK

June 15, 2020

Abstract

Nearly all life forms require iron to survive and function. Microorganisms utilize a number of mechanisms to acquire iron including the production of siderophores, which are organic compounds that combine with ferric iron into forms that are easily absorbed by the microorganism. There has been significant experimental investigation into the role, distribution and function of siderophores in fungi but until now no predictive tools have been developed to qualify or quantify fungi initiated siderophore-iron interactions. In this investigation we construct the first mathematical models of siderophore function related to fungi. Initially a set of partial differential equations are calibrated and integrated numerically to generate quantitative predictions on the spatio-temporal distributions of siderophores and related populations. This model is then reduced to a simpler set of equations that are solved algebraically giving rise to solutions that predict the distributions of siderophores and resultant compounds. These algebraic results require the calculation of zeros of cross products of Bessel functions and thus new algebraic expansions are derived for a variety of different cases that are in agreement with numerically computed values. The results of the modelling are consistent with experimental data while the analysis provides new quantitative predictions on the time scales involved between siderophore production and iron uptake along with how the total amount of iron acquired by the fungus depends on its environment. The implications to bio-technological applications are briefly discussed.

Key Words: mathematical model, partial differential equations, numerical solution, ferric iron uptake

*Corresponding author: graeme.boswell@southwales.ac.uk

1 Introduction

Iron is an essential element for nearly all life forms. In humans, iron deficiency can lead to several chronic medical conditions (such as anemia, Zimmermann and Hurrell, 2007; Beard, 2008), whereas in plants insufficient amounts of iron can severely hinder growth, which is particularly problematic since one third of the world's soils are considered to be iron deficient due to the insolubility of ferric iron present in the environment (Marschner, 1995). Indeed, nutritional iron is not readily available in the terrestrial environment and thus microorganisms have evolved mechanisms to cope with its scarcity by developing processes to convert and subsequently uptake iron to aid in their growth. These mechanisms have been studied at the molecular level for various microscopic eukaryotes including bacteria and pathogenic fungi (Philpott et al., 2012). In fungi, four different mechanisms for the acquisition of iron have been identified (e.g. Van der Helm and Winkelmann, 1994; Renshaw et al., 2002; Haas, 2014, and references therein) (i) Shuttle mechanism: ferric iron uptake mediated by ferric iron specific chelators (siderophores), (ii) Direct-transfer mechanism: reductive iron assimilation, (iii) Esterase-reductase mechanism: low-affinity ferrous iron uptake and (iv) Reductive mechanism: heme uptake and degradation. In this work we focus attention on the first, and most common, of these mechanisms. Under iron-limited conditions, many microorganisms produce and secrete small organic molecules called siderophores (Schwyn and Neilands, 1987; Saha et al., 2016). Siderophores are low molecular weight iron chelating compounds that move by Brownian motion and have a high affinity for ferric iron. Once the siderophores are attached to the ferric iron, the siderophore-iron complexes are transported by diffusion (Srivastava et al., 2013) and can be acquired by the organism, whereupon the iron is internalized and used to support further biomass growth and function.

Siderophores have drawn much attention in recent times due to their potential roles and applications in various bio-technologies including agriculture, ecology, bio-remediation, bio-control, bio-sensor and medicine (Saha et al., 2016). Their significance in applications are mainly due to siderophores having the ability to bind to a variety of metals in addition to iron (Bellenger et al., 2013; Braud et al., 2009; Sasirekha and Srividya, 2016). For example, siderophores play a crucial role in mobilizing metals from metal contaminated soils (Ahmed and Holmström, 2014, and references therein). Additionally in bio-control, microorganisms that produce certain siderophores can take up iron from around their immediate vicinity and invade a competitor's space in search for iron, which leads to the suppression of growth of several fungal pathogens (McLoughin et al., 1992; Verma et al., 2011).

Siderophores are classified by the ligands (an ion, molecule, or molecular group that binds to another chemical entity to form a larger complex) used to chelate the ferric iron that can be categorised as catecholates, hydroxamates, and carboxylates (Winkelmann, 1991, 2002; Ahmed and Holmström, 2014). Fungi mostly produce siderophores that fall in the "hydroxamates" category and most species of fungi make more than one type of siderophore, possibly to adapt to

different environmental conditions (Renshaw et al., 2002; Perez-Meranda et al., 2007; Johnson, 2008). Thus, various assays have been developed to detect the different phenotypes of siderophores. While these assays are useful for identifying various siderophores, numerous assays would have to be formed independently to detect all possible forms of siderophores, of which there are more than 500 known distinct types (Boukhalfa et al., 2003; Kraemer et al., 2005).

Schwyn and Neilands (1987) developed a universal siderophore detection assay using chrome azurol S (CAS) and hexadecyltrimethylammonium bromide (HDTMA) as visual indicators of the presence and function of siderophores. The CAS/HDTMA complexes tightly bond with ferric iron and become blue in colour. When a strong iron chelator, such as a siderophore, removes iron from the dye complex, the colour typically changes from blue to either orange, magenta or purple, depending on the exact assay (Bertrand et al., 2010). The toxicity induced by the HDTMA indicator can, in certain species, inhibit and even prevent the normal growth and function of the fungus (Schwyn and Neilands, 1987). Consequently numerous later studies (e.g. Milagres et al., 1999) have been based around a split Petri dish where the HDTMA indicator is added to one semi-circular region but absent from the other half; such configurations have been successfully modelled by one of the authors (Choudhury, 2019).

Despite their widespread existence, there has been relatively little attempt at the mathematical modelling of siderophores and their interaction with iron. In fungi, their mathematical treatment has typically been focussed on quantifying siderophore extent using simple ad-hoc approaches, such as measuring the physical distance of the colour change on a Petri dish or placing square paper underneath the Petri dish and recording the change in area over a time period (Machuca and Milagres, 2003; Bogumiłet al., 2013; Ghosh et al., 2015; Andrews et al., 2016a,b). However, siderophores produced by bacteria have received more advanced mathematical treatment, typically using sets of differential equations (e.g. Eberi and Collinson, 2009; Niehus et al., 2017). Leventhal et al. (2019) developed the most insightful mathematical model by considering siderophores produced from a single non-moving and isolated bacteria cell and their subsequent interaction with iron in a marine environment to form siderophore-iron complexes and represented this process using a simple reaction-diffusion equation.

Consequently, and given the sheer volume of applications involving fungi described above, it is timely that such a mathematical modelling exercise is performed that focuses on siderophore production involving an expanding fungal colony and thus significantly extending previous treatments of siderophore function. In this article a set of partial differential equations is developed that model the growth of a fungal biomass in response to nutrients and which produces siderophores to acquire iron from the external environment. The models are less concerned with how the biomass subsequently uses the iron; rather the models predict the quantity of iron acquired by the biomass and how iron is distributed in the external environment as a result of siderophore interactions, and thus provides quantitative predictions related to the experimental protocols described above. A mathematical model is developed in Section 2 that simulates

the growth of a mycelium, the production of siderophores and their resultant interaction with iron in a planar domain, representing typical experimental protocol corresponding to the growth of a fungus in a Petri dish. The effect of different concentrations of iron and external nutrients are investigated by solving the equations numerically. These simulations motivate the construction of a simplified set of equations, considered in Section 3, that focus on the siderophore dynamics. Algebraic solutions are constructed that describe the temporal evolution of the siderophore dynamics towards a steady state distribution and are consistent with the numerical approach. These algebraic solutions make use of various asymptotic expansions applied to cross-products of Bessel functions and hence new results and methods are developed accordingly. The implications of the results and future work are discussed in Section 4.

2 Siderophore-iron interactions from an expanding biomass

2.1 Model equations

Due to the dense network structure of a fungal mycelium, a continuum approach is used to model its growth in a planar setting, representing mycelial expansion in a Petri dish. The growth and function of a fungus in such settings has been previously modelled by Boswell et al. (2003) and expanded upon in a series of papers (e.g. Boswell et al., 2007; Choudhury et al., 2018, and references therein). In short, a fungal mycelium comprises a network of tubes, termed hyphae, that can branch, extend at their unbounded ends, fuse with other hyphae (anastomosis), acquire new growth material from the external environment (uptake) and redistribute that material through the network (translocation). For the purposes of modelling, the mycelium is assumed to comprise three variables representing active hyphae (denoted by ρ and corresponding to those hyphae involved in nutrient uptake, branching, anastomosis and translocation), inactive hyphae (denoted by ρ' corresponding to hyphae no longer involved in colony function but still remaining part of the mycelium), and hyphal tips (denoted by n) representing the expanding ends of active hyphae. Briefly, hyphal tips move predominantly in a straight line but with some random variations which is modelled by an advective process directed away from hyphae coupled with a diffusive process representing the random reorientation. (This growth characteristic is a consequence of the delivery of vesicles from the Spitzenkörper to the hemiellipsoid-shaped apical tip, Riquelme et al., 2018). New hypha are therefore formed from the trail left behind a tip as it moves and thus the tip flux corresponds to the creation of hyphal biomass. Thus the absolute value of the flux is a convenient approximation of the amount of new material created through the movement of hyphal tips. Tips are created through branching along existing active hyphae and are lost through anastomosis also with active hyphae. It is assumed that a single generic substrate is responsible for growth. This substrate exists in two forms; external to the mycelium (with density s_e) and held within

the mycelium (with density s_i). The external substrate may represent combinations of carbon, nitrogen and trace metals other than iron while the internalised substrate additionally includes iron. Internally-located substrate is translocated through the biomass structure by a combination of diffusion and active transport directed towards the hyphal tips, the latter of which has a metabolic cost and there is a further cost associated with the movement of hyphal tips. Consistent with experimental evidence, tip flux and branching rates increase with the internal substrate (Gruhn et al., 1992) and this resource is also used to uptake external substrate.

It is assumed that the biomass is in an iron-depleted state and thus siderophores are being released throughout its extent. Consistent with the nutrient uptake process, it is assumed siderophore production can only arise in the presence of sufficient energy reserves, and in the absence of experimental evidence to the contrary, it is assumed that siderophore production is proportional to the internal substrate concentration and the density of active biomass with r_1 denoting the constant of proportionality. When released to the external environment, siderophores (denoted by C) diffuse and bind with iron (denoted by I) to form siderophore-iron complexes (denoted by V) and standard enzyme-reaction kinetics are assumed to describe this binding process with r_2 denoting the rate constant. These complexes subsequently diffuse and are absorbed by the biomass across hyphal cell walls. As previously mentioned, there are in excess of 500 different types of siderophores with quantitatively and qualitatively different characteristics and consequently there are a multitude of different pathways via which the fungus acquires iron from the siderophore-iron complexes (Howard, 1999; Winkelmann, 2007). Simple diffusion across the hyphal cell wall is common to all and hence this process is used to account for the iron uptake, where r_3 is the uptake rate constant. Once internalized, the iron forms a component of the generic internal substrate that is subsequently used to promote further growth via hyphal tip extension and translocation, and to acquire additional resources, including more iron. The uptake and subsequent conversion of the siderophore-iron complex into the generic internalised substrate has an associated cost and hence the effective acquisition rate of the complex, r_3', is less than the overall uptake rate, r_3. Thus the entire system can be modelled using the mixed hyperbolic-parabolic set of partial differential equations given by

$$\rho_t = |v s_i n \nabla\rho + D_n s_i \nabla n| - d_\rho \rho, \tag{2.1a}$$

$$\rho_t' = d_\rho \rho - d_i \rho', \tag{2.1b}$$

$$n_t = \nabla \cdot (v s_i n \nabla\rho + D_n s_i \nabla n) + \alpha s_i \rho - \beta n \rho, \tag{2.1c}$$

$$\begin{aligned} s_{i_t} = {} & \nabla \cdot (D_i \rho \nabla s_i - D_a \rho s_i \nabla n) + c_1 \rho s_i s_e - c_2 \left| v s_i n \nabla\rho + D_n s_i \nabla n \right| \\ & - c_4 \left| D_a \rho s_i \nabla n \right| - r_1 \rho s_i + r_3' V \rho, \end{aligned} \tag{2.1d}$$

$$s_{e_t} = D_e \nabla^2 s_e - c_3 \rho s_i s_e, \tag{2.1e}$$

$$I_t = D_I \nabla^2 I - r_2 I C, \tag{2.1f}$$

$$C_t = D_C \nabla^2 C + r_1' \rho s_i - r_2 I C, \tag{2.1g}$$

$$V_t = D_V \nabla^2 V + r_2 I C - r_3 V \rho. \tag{2.1h}$$

The model variables and parameters along with their calibrated values are given in Tables 1 & 2 respectively.

Variable	*Description*	*Unit*
ρ	active hyphal density	cm^{-1} (cm hyphae cm^{-2})
ρ'	inactive hyphal density	cm^{-1} (cm hyphae cm^{-2})
n	hyphal tip density	tips cm^{-2}
s_i	internal substrate concentration	mol cm^{-2}
s_e	external substrate concentration	mol cm^{-2}
I	concentration of free iron	mol cm^{-2}
C	concentration of siderophores	mol cm^{-2}
V	concentration of siderophore-iron complex	mol cm^{-2}

Table 1: Summary of model variables used in equation (2.1)

The flux term in equation (2.1c) corresponds to the motion of hyphal tips accounting for their straight line growth habit (where s_i accounts for the role of the growth promoting substrate in the process) coupled with variations about this orientation, modelled using diffusion. The parameter v, corresponding to the straight line growth habit of individual hyphae, is influenced by toxicity in the external environment; in particular, tip extension can be inhibited through the presence of the HDTMA visual indicator used to detect the presence of siderophores (Schwyn and Neilands, 1987). Indeed, numerous studies (e.g. Fomina et al., 2000) have shown that the ability of fungi to colonize space occupied by toxic material is increased through the availability of nutrients such as carbon. Consequently, it is tacitly assumed that the HDTMA indicator is uniformly distributed and at a concentration that does not prevent the biomass from expanding so that v may be regarded as a positive constant and thus the expansion of the model biomass into the space where the HDTMA visual indicator is present is consistent with experimental observations. Furthermore this phenomenon further justifies the explicit modelling of both an external substrate, representing nutrients that assist the fungi in overcoming the toxicity, and the iron distribution. The metabolic cost of tip movement is accounted for in equation (2.1d) through the parameter c_2, while the trail left behind the tip, and thus the creation of new hyphae, is given by the related term in equation (2.1a). The flux in equation (2.1d) represents movement of internally-held material through the network (i.e. translocation) having both diffusive and directed components, the latter towards hyphal tips and having a metabolic cost. Equations (2.1a)–(2.1e) are precisely those in Boswell et al. (2003). In equations (2.1f)-(2.1h) the iron, siderophore and the siderophore-iron complex populations are assumed to undergo standard Fickian diffusion with coefficients D_I, D_C and D_V respectively. Note that the key function of siderophores is to increase the mobility of iron, which is achieved through the formation of siderophore-iron complexes. Thus $D_I < D_V$. See Howard (1999) and Leventhal et al. (2019) for further details

and discussion of calibration.

Equations (2.1) are considered on a domain representing a typical experimental protocol, i.e. a circular Petri dish of radius R_{dish} with an initially uniform growth medium inoculated at its centre by a small circular plug of biomass of radius R_{plug}. Consequently the biomass is initially confined to a central region of the domain with no siderophore or siderophore-iron complexes. Thus the initial data is

$$[\rho, \rho', n, s_i, s_e, I, C, V] = \begin{cases} [\rho_0, 0, n_0, s_{i_0}, s_{e_0}, I_0, 0, 0] & \text{if } r < R_{plug}, \\ [0, 0, 0, 0, s_{e_0}, I_0, 0, 0] & \text{otherwise,} \end{cases} \tag{2.2}$$

where r denotes the distance from the centre of the domain (i.e. the inoculation site) while zero-flux boundary conditions are applied on the boundary $r = R_{dish}$ for all model variables.

2.2 Numerical solutions

The model equations (2.1) with initial data (2.2) were solved using Comsol Multiphysics. Parameter values and initial data were used from the calibrations in Boswell et al. (2002, 2003); Perez-Meranda et al. (2007); Eberi and Collinson (2009); Leventhal et al. (2019) while reasonable assumed values were taken for the complex uptake rate r_3 (Table 2). A typical solution is shown in Fig. 1.

Parameter	*Value*	*Description*	*Unit*
v	0.5	tip velocity[2]	$\text{cm}^5\ \text{day}^{-1}\ \text{mol}^{-1}$
D_n	0.1	tip diffusion[2]	$\text{cm}^4\ \text{day}^{-1}\ \text{mol}^{-1}$
d_ρ	0.2	hypha inactivation rate[1]	day^{-1}
d_i	0	inactive hypha decay rate[1]	day^{-1}
α	10 000	branching rate[2]	$\text{cm mol}^{-1}\ \text{day}^{-1}$
β	10 000	anastomosis rate[2]	cm day^{-1}
D_i	10	internal substrate diffusion coefficient[2]	$\text{cm}^3\ \text{day}^{-1}$
D_a	10	internal substrate active transport[2]	$\text{cm}^5\ \text{day}^{-1}$
c_1	900	nutrient uptake rate[1]	$\text{cm}^3\ \text{mol}^{-1}\ \text{day}^{-1}$
c_2	1	tip extension costs[1]	mol cm^{-1}
c_3	1000	nutrient uptake rate[1]	$\text{cm}^3\ \text{mol}^{-1}\ \text{day}^{-1}$
c_4	10^{-8}	active translocation costs[2]	cm^{-1}
D_e	0.0001	external substrate diffusion coefficient[1]	$\text{cm}^2\ \text{day}^{-1}$
D_I	0.000864	iron diffusion coefficient[4]	$\text{cm}^2\ \text{day}^{-1}$
D_C	0.3	siderophore diffusion coefficient[5]	$\text{cm}^2\ \text{day}^{-1}$
D_V	0.3	complex diffusion coefficient[5]	$\text{cm}^2\ \text{day}^{-1}$
r_1	10^{-7}	siderophore production costs[5]	cm day^{-1}
r_1'	100	production of siderophores[5]	cm day^{-1}
r_2	100	complex production rate[5]	$\text{cm}^2\ \text{mol}^{-1}\ \text{day}^{-1}$
r_3	1000	complex uptake rate	cm day^{-1}
r_3'	900	conversion of iron to substrate	cm day^{-1}
R_{dish}	2	radius of Petri dish	cm
R_{plug}	0.2	radius of inoculum[1]	cm
ρ_0	0.1	initial biomass density[1]	cm^{-1}
n_0	0.1	initial tip density[1]	cm^{-2}
s_{i_0}	0.4	initial internal substrate density [1]	mol cm^{-2}
s_{e_0}	0.6	initial external substrate density [1]	mol cm^{-2}
I_0	0.004	initial iron concentration[3]	mol cm^{-2}

Table 2: Parameter values used in model equations (2.1) with initial data (2.2). The values are taken from [1]Boswell et al. (2002), [2]Boswell et al. (2003), [3]Perez-Meranda et al. (2007), [4]Eberi and Collinson (2009), [5]Leventhal et al. (2019) while the remaining parameters were assumed to take values consistent with those in similar processes. The value of R_{dish} was chosen to represent a Petri dish of radius 2 cm for computational convenience.

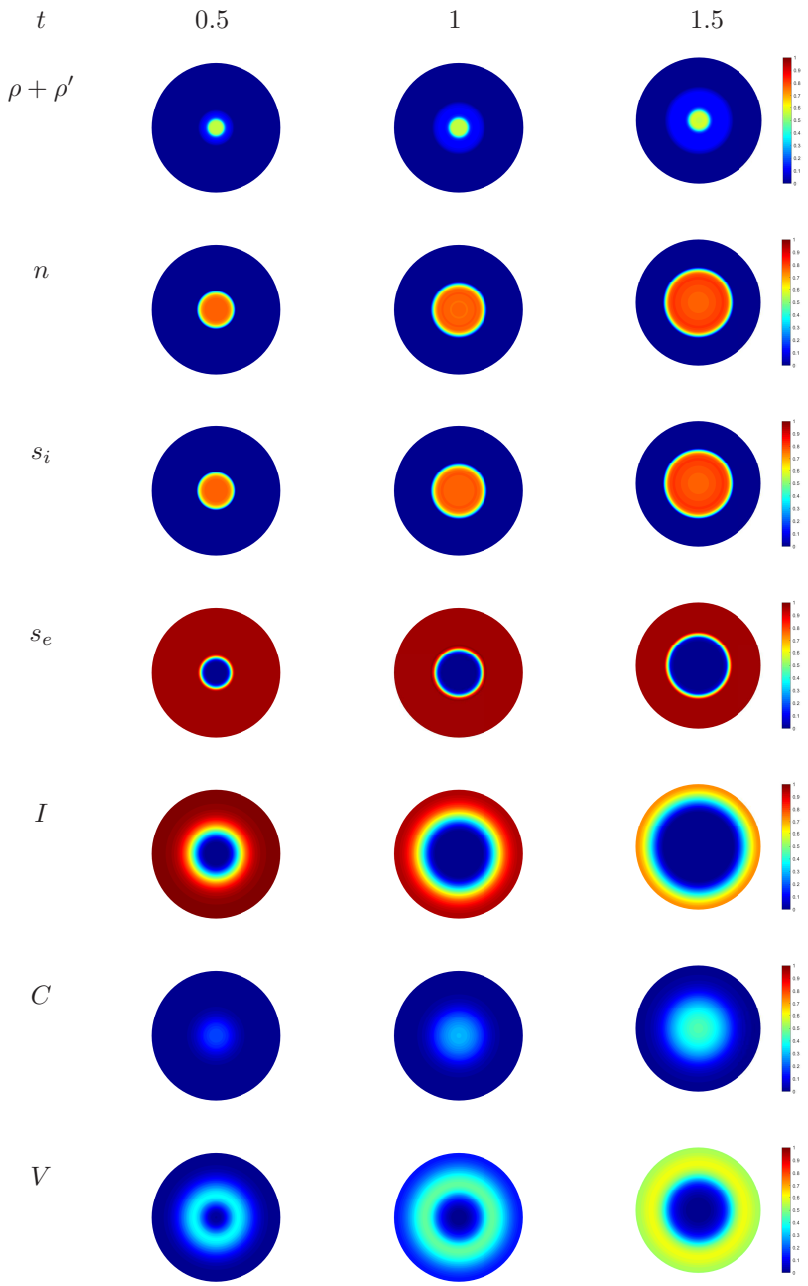

Figure 1: Numerical solution of equations (2.1) with initial data (2.2) at times $t = 0.5, 1, 1.5$ (representing days) over a circular domain with representative diameter 4 cm. Parameter values are given in Table 2. For each variable, the colour range is shown as a proportion of their maximum value between times $t = 0$ and $t = 3$ (i.e. when the biomass had collided with the edge of the domain).

The model biomass expanded outwards in a radially-symmetric manner and was preceded by an increased density of model tips. The external substrate was depleted in regions occupied by the biomass. Indeed, the numerical solutions for these variables mirrored those in Boswell et al. (2003), indicating the validity of the numerical integration scheme utilised in the current study, and therefore are consistent both qualitatively and quantitatively with experimental data on the growth of a mycelium in initially uniform nutrient settings (see Boswell et al., 2003, and references therein).

The siderophore population was greatest at the centre of the domain and expanded beyond the extent of the biomass. The iron distribution was depleted from the middle of the domain outwards and the extent of the depletion exceeded the range of the model biomass. The resultant siderophore-iron complex distribution was greatest in the zone between the model biomass and where the iron population was at its greatest and thus consistent with the complex's formation where siderophores first encounter iron and where the complex is absorbed by the biomass.

While the quantitative concentrations of the siderophores and the siderophore-iron complex cannot be related to experimental data, the depletion of the iron population has the same qualitative features as observed in numerous experiments (e.g. Milagres et al., 1999; Bertrand et al., 2010; Srivastava et al., 2013); namely iron is depleted in a radially symmetric fashion and this depletion extends beyond the extremes of the fungal biomass. Indeed, the formation of the siderophore-iron complex coincides with the depletion of iron and hence the extent of the complex V from the biomass periphery yields information on the magnitude of the zone within which the siderophores operate.

2.2.1 Variations in initial iron concentration

The extent of the biomass, siderophores, iron and siderophore-iron complexes depend on the concentration of iron as shown in Fig. 2. The extent is defined to be the boundary where each concentration is equal to a critical level (stated in the figure legend) and since the siderophore-iron complex advances as a "ring" formation, both the inner and outer boundaries of that structure are shown. In all cases, the extent of the biomass increases approximately linearly over time, indicative of a constant growth rate, and this also marginally increases with I_0, consistent with the use of that resource to further promote growth, and therefore has similar characteristics to other modelling investigations and experimental results (e.g., Prosser and Trinci, 1979, where tip vesicles are analogous to internal substrate). The siderophore and iron extent both decline with increasing iron concentration because of the concomitant increased rate of complex formation. Consequently, the extent of the complexes increases with the initial iron concentration I_0 so that whereas for reduced initial iron concentrations the complexes are only found in the vicinity of the biomass edge (Fig. 2(a)), for greater concentrations the complexes are found throughout most of the domain (e.g. Fig, 2(c)). This observation significantly extends experimental results that focus only on the uptake of iron from the growth medium and, due to the diffi-

culties in tracking siderophores, not their distribution prior to or after forming the iron complexes. Throughout Fig. 2, the sudden increase in the extent of the siderophore and siderophore-iron complex populations close to $r = 2$ is due to their interactions with the boundary at $r = 2$.

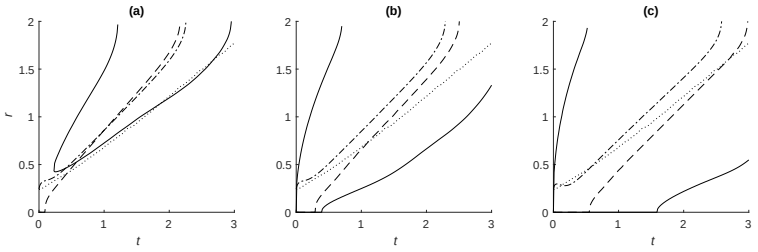

Figure 2: The distance r at times t from the centre of the domain where $\rho + \rho'$ (dotted), C (dot-dashed), I (dashed) and V (solid) take critical values for differing concentrations of iron. (a) $I_0 = 0.0004$, (b) $I_0 = 0.004$, (c) $I_0 = 0.04$ representing one tenth, one and ten times the calibrated initial iron value. (Notice that the complex V expands as a "ring" and hence its inner and outer extents are shown.) The critical concentrations are defined to be 0.0181 for biomass, 4×10^{-5} for iron, 0.0679 for siderophores, and 1.204×10^{-4} for the complex, representing one tenth of their maximum values for the numerical solution with $I_0 = 0.0004$.

2.2.2 Variations in initial external substrate concentration

The extent of the biomass, siderophores, iron and siderophore-iron complex are strongly influenced by the concentration of the external substrate as shown in Fig. 3. Firstly, the extent of the biomass increased with the external substrate due to the increased uptake, branching and model tip extension associated with that resource with the least external substrate corresponding to minimal biomass expansion (Fig. 3(a)), consistent with widely-reported data relating fungal growth and productivity to nutrient availability (e.g. Suberkropp, 2011). Additionally, since siderophores are produced at a rate proportional to the internal substrate, the siderophore extent also increased with the external substrate, with the initial internal substrate concentration responsible for an initial but not sustained production of siderophores under reduced external substrate concentrations (Fig. 3(a)). The depletion of the iron increased with the external substrate but not linearly; a ten-fold reduction from the default value of s_{e_0} (Fig. 3(c)) did not result in a ten-fold reduction of the extent of iron (Fig. 3(a)). However, the distribution of the siderophore-iron complexes displayed a highly irregular association with the external substrate. For low concentrations of the external substrate, the complex distribution arose as a narrow "ring" a significant distance away from the biomass periphery (Fig. 3(a)). However, as the external substrate increased, the width of this "ring" increased through a reduction in its inner radius (Fig. 3(b)). As the external substrate concentration

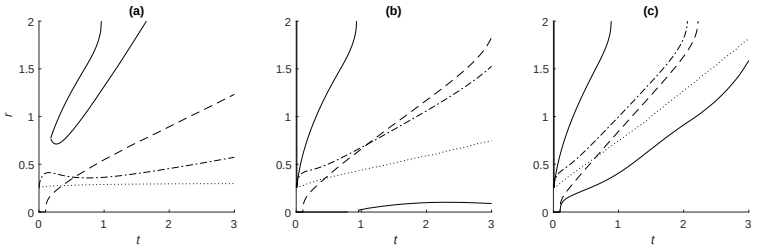

Figure 3: The distance r at times t from the centre of the domain where $\rho + \rho'$ (dotted), C (dot-dashed), I (dashed) and V (solid) take critical values for differing concentrations of external substrate. (a) $s_{e_0} = 0.06$, (b) $s_{e_0} = 0.3$, (c) $s_{e_0} = 0.6$ representing one tenth, one half and one multiple of the calibrated value. (Notice that the complex V expands as a "ring" and hence its inner and outer extents are shown.) The critical concentrations are defined to be 0.01 for biomass, 4×10^{-4} for iron, 0.04 for siderophore, and 3.341×10^{-4} for the complex, representing one tenth of their maximum values for the numerical solution with $s_{e_0} = 0.06$.

increased still further, the inner radius of the "ring" expanded and thus reduced the region of the domain in which the complexes were greatest in concentration (Fig. 3(c)). This nonlinear change in siderophore-iron complex distributions due to external substrate concentrations is likely because of associated variations in the production of siderophores coupled with the formation of the complexes and their subsequent uptake by the biomass. For large concentrations of the external substrate, not only were large amounts of siderophores produced, but also the biomass expanded quickly that enabled a more rapid uptake of siderophore-iron complexes. On the other hand, for reduced concentrations of the external substrate, fewer siderophores were produced, the production of siderophore-iron complexes was thus reduced and their subsequent uptake by the biomass was delayed since biomass expansion was slower.

2.2.3 Cumulative iron uptake

As previously explained, micro-organisms produce siderophores to acquire iron only when in an iron-deficient state. Consequently, quantitative predictions on the amount of iron obtained by the biomass through the acquisition of the iron-siderophore complexes is fundamental in this model. (Indeed, when the internalized iron concentration reaches such a critical level then siderophore production is ceased.) It has previously been shown that the extent of biomass, siderophores and siderophore-iron complexes depends on the initial concentration of iron and external substrate which will therefore also impact on the ultimate uptake of iron by the biomass.

Due to the structure of the model equations, iron is either free in the external environment, combined as complexes with siderophores, or has been taken up

by the model biomass. Consequently the cumulative amount of iron acquired by the model biomass at time t can be easily calculated by considering the difference between the initial iron population and the amount of iron at time t existing in either their free form (i.e. denoted by I) or that currently held in complexes (i.e. denoted by V):

$$\text{cumulative iron uptake by time } t = \int_\Omega I_0(x,y)\,\mathrm{d}\Omega - \int_\Omega I(x,y,t)\,\mathrm{d}\Omega - \int_\Omega V(x,y,t)\,\mathrm{d}\Omega \tag{2.3}$$

where Ω denotes the entire domain (i.e. the region inside the Petri dish).

The cumulative amount of iron obtained by the biomass depended upon the initial amount of iron in the external environment and on the external substrate (Fig. 4). In all instances, there was a sudden increase in the quantity of internally-held iron and the rate of increase subsequently declined until boundary effects impacted on this process (approximately at time $t = 2$ for the simulations with large values of I_0 and s_{e_0}). While there appears to be a near linear relationship between the amount of iron in the external environment and that subsequently obtained by the biomass (Fig. 4(a)), there is a more complex non-linearity between the external substrate concentrations and the amount of iron obtained where a ten-fold reduction in external resources only approximately halves the total amount of iron acquired by the biomass (Fig. 4(b)).

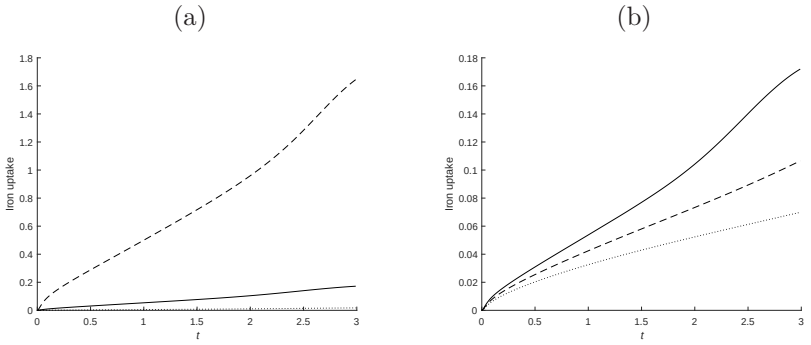

Figure 4: The cumulative amount of iron obtained by the biomass. (a) The initial iron concentration is varied where $I_0 = 0.004$ (solid line), $I_0 = 0.04$ (dashed line), $I_0 = 0.0004$ (dotted line) and in all cases $s_{e_0} = 0.6$. (b) The initial external substrate is varied where $s_{e_0} = 0.6$ (solid line), $s_{e_0} = 0.3$ (dashed line), $s_{e_0} = 0.06$ (dotted line) and in all cases $I_0 = 0.004$.

3 Siderophore-complex distributions: an algebraic approach

The analysis in the previous section essentially focussed on the temporal change in the distances over which the siderophores operated and generated good qual-

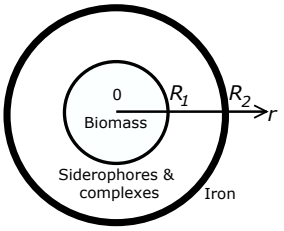

Figure 5: The circular fungal biomass has radius R_1 centred at the origin while the iron is contained outside the circular region of radius R_2. The siderophores and the siderophore-iron complexes exist in the "ring" between the two circles. Siderophores are released from the biomass at $r = R_1$, are converted into complexes at $r = R_2$, and the complexes are subsequently taken up by the biomass at $r = R_1$.

itative agreement with experimental observations (Milagres et al., 1999; Srivastava et al., 2013). In polluted terrestrial environments, combinations of heavy metals and other toxins may be present that inhibit the growth of a fungus (Fomina et al., 2000), in addition to toxicity from the HDTMA visual indicator. In such cases, while siderophores are still released by fungi in an iron-depleted state, the mycelium does not necessarily expand due to the presence of pollutants. Since the standard experimental approach to observing siderophore dynamics relates to observing the reduction in iron from the growth medium, if the initial iron concentration is sufficiently high then small losses may not be visually observable. Here a simplification of model equations (2.1) is used to construct quantitative predictions on siderophore and siderophore-iron complexes in such settings.

It is assumed that a circular biomass in an iron-depleted state is positioned inside a toxic region that prohibits its subsequent expansion. This could represent a situation where a fungus is introduced to a domain exhibiting large concentrations of heavy metals, which, for example, arises in bio-remediation applications. Distributions of iron are positioned outside of the toxic region and therefore siderophores provide the sole means of the biomass obtaining iron. See Fig. 5 for a schematic illustration. A key aspect of this investigation is the distance between the biomass, where the siderophores are produced, and the iron resource, where the complexes are formed. Thus the radius of the biomass, R_1, and the distance of the iron from the centre of the biomass, R_2, are crucial parameters. The biomass is assumed to release siderophores at a constant rate that subsequently diffuse. Since it is reasonable to assume the diffusive time scale is greater than the reactive time scale, once the siderophores encounter the distribution of iron a siderophore-iron complex is immediately formed and diffuses. When the complex reaches the biomass it is immediately absorbed so that the iron can be utilized by the biomass. Consequently the above scenario can be represented using polar coordinates and due to radial symmetry (see also the results in Section 2) there is no variation with the angular coordinate. Thus,

consistent with the above approaches, the siderophore population is governed by

$$\frac{\partial C}{\partial t} = \frac{D_c}{r}\frac{\partial}{\partial r}\left(r\frac{\partial C}{\partial r}\right) \qquad \text{for } R_1 < r < R_2. \tag{3.1}$$

Since siderophores are released at a constant rate by the biomass and immediately form siderophore-iron complexes once the iron distribution is encountered, the corresponding boundary conditions are

$$D_c\frac{\partial C}{\partial r}(R_1, t) = -k, \qquad C(R_2, t) = 0, \tag{3.2}$$

where the flux k corresponds to the rate siderophores enter the region $R_1 < r < R_2$ from the biomass. It is useful to note that boundary condition (3.2) on $r = R_1$ is an alternative but eventually equivalent condition obtained from the solution of

$$\begin{aligned} \frac{\partial C}{\partial t} =& \frac{D_c}{r}\frac{\partial}{\partial r}\left(r\frac{\partial C}{\partial r}\right) + \frac{2k}{R_1}H(R_1 - r), \qquad \text{for } 0 < r < R_2, \\ & \frac{\partial C}{\partial r}(0, t) = 0, \qquad C(R_2, t) = 0, \end{aligned} \tag{3.3}$$

where H denotes the standard Heaviside step function and represents the case where siderophores are produced throughout the region $r < R_1$ at a constant rate so that after a transient time the flux at $r = R_1$ is a constant $-\frac{k}{D_c}$. For convenience we use boundary condition (3.2) but will later exploit (3.3) in Section 3.1.2.

It is assumed that initially there are no siderophores in the domain, i.e.

$$C(r, 0) = 0. \tag{3.4}$$

The siderophore-iron complex also undergoes diffusion and hence is modelled using

$$\frac{\partial V}{\partial t} = \frac{D_v}{r}\frac{\partial}{\partial r}\left(r\frac{\partial V}{\partial r}\right) \qquad \text{for } R_1 < r < R_2. \tag{3.5}$$

The siderophore-iron complex forms immediately upon interaction between the siderophores and the iron distribution. Half the resultant complex continues to diffuse in the outward direction while the other half diffuses back towards the biomass whereupon it is immediately absorbed. Thus the boundary conditions are given by

$$V(R_1, t) = 0, \qquad D_v\frac{\partial V}{\partial r}(R_2, t) = -\frac{1}{2}D_c\frac{\partial C}{\partial r}(R_2, t). \tag{3.6}$$

It is assumed that at time $t = 0$ there are no siderophore-iron complexes in the domain and so the initial data is

$$V(r, 0) = 0. \tag{3.7}$$

Notice that equations (3.1) and (3.5) are similar to annihilation models (e.g. Ben-Haim and Redner, 1992) except the annihilation arises from a boundary condition rather than a reaction.

It is advantageous to nondimensionalise the model equations before constructing their solution. By introducing $t^* = \frac{D_v}{R_1^2}t$, $r^* = \frac{r}{R_1}$, $R = \frac{R_2}{R_1}$, $D = \frac{D_c}{D_v}$, $C^* = \frac{D_v C}{kR_1}$ and $V^* = \frac{2D_v V}{kR_1}$ the model equations reduce to

$$\frac{\partial C}{\partial t} = \frac{D}{r}\frac{\partial}{\partial r}\left(r\frac{\partial C}{\partial r}\right), \qquad \text{for } 1 < r < R, \tag{3.8a}$$

$$\frac{\partial V}{\partial t} = \frac{1}{r}\frac{\partial}{\partial r}\left(r\frac{\partial V}{\partial r}\right), \qquad \text{for } 1 < r < R, \tag{3.8b}$$

with boundary conditions and initial data

$$D\frac{\partial C}{\partial r}(1,t) = -1, \qquad V(1,t) = 0, \tag{3.9a}$$

$$C(R,t) = 0, \qquad D\frac{\partial C}{\partial r}(R,t) = -\frac{\partial V}{\partial r}(R,t), \tag{3.9b}$$

$$C(r,0) = V(r,0) = 0 \tag{3.9c}$$

and where $^*s$ have been dropped for notational convenience.

The solutions of equations (3.8) with the initial data and boundary conditions (3.9) are in Appendix A shown to be

$$\begin{aligned} C(r,t) &= \frac{1}{D}\ln\left(\frac{R}{r}\right) + \sum_{n=1}^{\infty} A_n \phi_n(r) e^{-\lambda_n D t}, \\ V(r,t) &= \ln(r) - D\sum_{n=1}^{\infty} A_n \frac{\phi_n'(R)}{\psi_n'(R)}\psi_n(r)e^{-\lambda_n D t} + \sum_{n=1}^{\infty} E_n \omega_n(r) e^{-\mu_n t}, \end{aligned} \tag{3.10}$$

where the eigenvalues λ_n and μ_n are the roots of the characteristic equations

$$\begin{aligned} \frac{J_1\left(\sqrt{\lambda_n}\right)}{J_0\left(\sqrt{\lambda_n}R\right)} - \frac{Y_1\left(\sqrt{\lambda_n}\right)}{Y_0\left(\sqrt{\lambda_n}R\right)} &= 0, \\ \frac{J_1\left(\sqrt{\mu_n}R\right)}{J_0\left(\sqrt{\mu_n}\right)} - \frac{Y_1\left(\sqrt{\mu_n}R\right)}{Y_0\left(\sqrt{\mu_n}\right)} &= 0, \end{aligned} \tag{3.11}$$

respectively, the eigenfunctions $\phi_n(r)$, $\psi_n(r)$ and $\omega_n(r)$ are given by

$$\begin{aligned} \phi_n(r) &= \frac{Y_0\left(\sqrt{\lambda_n}r\right)}{Y_0\left(\sqrt{\lambda_n}R\right)} - \frac{J_0\left(\sqrt{\lambda_n}r\right)}{J_0\left(\sqrt{\lambda_n}R\right)}, \\ \psi_n(r) &= \frac{Y_0\left(\sqrt{\lambda_n D}r\right)}{Y_0\left(\sqrt{\lambda_n D}\right)} - \frac{J_0\left(\sqrt{\lambda_n D}r\right)}{J_0\left(\sqrt{\lambda_n D}\right)}, \\ \omega_n(r) &= \frac{Y_0\left(\sqrt{\mu_n}r\right)}{Y_0\left(\sqrt{\mu_n}\right)} - \frac{J_0\left(\sqrt{\mu_n}r\right)}{J_0\left(\sqrt{\mu_n}\right)}, \end{aligned}$$

where J_m and Y_m $(m = 0, 1)$ are the Bessel functions of the first and second kind respectively, and A_n and E_n are given by

$$A_n = \frac{2\phi_n(1)}{D\left[\phi_n^2(1)\lambda_n - R^2(\phi_n'(R))^2\right]},$$

$$E_n = \frac{2\omega_n(R)\left[1 - R\mu_n D\sum_{m=1}^{\infty}\frac{A_m\phi_m'(R)}{\mu_n - D\lambda_m}\right]}{\left(\omega_n'(1)\right)^2 - \mu_n R^2\omega_n^2(R)},$$

provided $\mu_n \neq D\lambda_m$ for all eigenvalues μ_n and λ_m. Notice that the eigenvalues λ_n and μ_n from equation (3.11) correspond to the zeros of a cross product of Bessel functions, which have long been studied (e.g. Fettis and Caslin, 1966).

3.1 Results using numerically computed eigenvalues

The eigenvalues in equation (3.11) were computed numerically in Matlab enabling the calculation of solutions in (3.10). Since these solutions involve generalised Fourier series, in the investigations below, the summations in equations (3.10) are truncated after 10 terms since the inclusion of further terms produced graphically indistinguishable results.

3.1.1 Typical results

The temporal changes in the distributions of the siderophore and siderophore-iron complexes, as obtained from equation (3.10), are shown in Fig. 6. Initially both distributions are zero throughout the domain. Due to the influx of siderophores at the $r = 1$ boundary, the distribution of siderophores increases accordingly. After a sufficient time has passed, the siderophore population has extended across the domain to reach the $r = R$ boundary. Accordingly, the production of the siderophore-iron complexes is initiated and this continues to increase so that the complexes subsequently diffuse back across the domain where they are absorbed at the $r = 1$ boundary. As expected, the siderophore distribution approaches its steady state prior to that of the siderophore-iron complex distribution and where the steady states $C_S(r)$ and $V_S(r)$ are respectively given by the leading terms in equation (3.10), i.e.

$$C_S(r) = \frac{1}{D}\ln\left(\frac{R}{r}\right), \qquad V_S(r) = \ln(r), \qquad \text{for } 1 < r < R. \quad (3.12)$$

Thus increases in R, representing the relative difference between the location of the iron and the extent of the biomass, results in increases in the density of both the siderophore and the siderophore-iron complex throughout the domain.

3.1.2 Siderophore-complex distribution: numerical predictions

The above algebraic solution can be compared to the numerical solutions of model equations (2.1). To simulate the configuration in Fig. 5, R_{dish} was taken

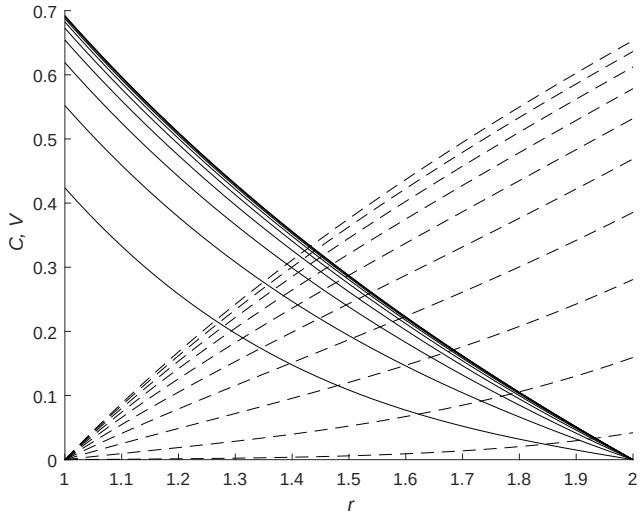

Figure 6: The distribution of siderophores C (solid lines) and siderophore-iron complexes V (dashed lines) from equation (3.10) with $D = 1$ and $R = 2$ are shown at times $t = 0, 0.2, 0.4, \ldots, 2$.

to be 0.45 and the iron was located in the region within a distance 0.05 of the boundary of that boundary so that $R_2 = 0.4$ and $R_1 = R_{plug} = 0.2$ as before. To represent large concentrations of iron, the calibrated value of I_0 in Table 2 was increased 100 fold and was assumed to be continually replenished upon the production of siderophore-iron complexes and was implemented by removing the corresponding depletion term in equation (2.1f). Finally, the biomass was prevented from expanding from its initial distribution by setting both v and D_n to be zero.

To best compare the output of the full model equations (2.1) to the algebraic solutions (3.10), note that the siderophore population in equation (2.1g) can be approximated by (3.3) and that after the same nondimensionalisation described above the steady state solution is

$$C(r) = \begin{cases} \frac{1+2\ln(R)-r^2}{2D}, & \text{for } 0 < r < 1, \\ \frac{1}{D}\ln\left(\frac{R}{r}\right), & \text{for } 1 < r < R, \end{cases}$$

and therefore satisfies $D\frac{\partial C}{\partial r}(1) = -1$, consistent with equation (3.9a). Using this approach it is seen that the siderophore and siderophore-iron complex populations develop in a similar way to that seen previously (Fig. 7). Indeed, the main difference between the numerical and algebraic solutions arises at $r = 1$ for small times due to the immediate uptake of siderophore-iron complex in the latter (via boundary condition (3.9a)) compared to a more prolonged process in the former (represented by the reaction term in equation (2.1h)). Thus there is

clearly a strong qualitative and quantitative agreement between the algebraic and numerical solutions.

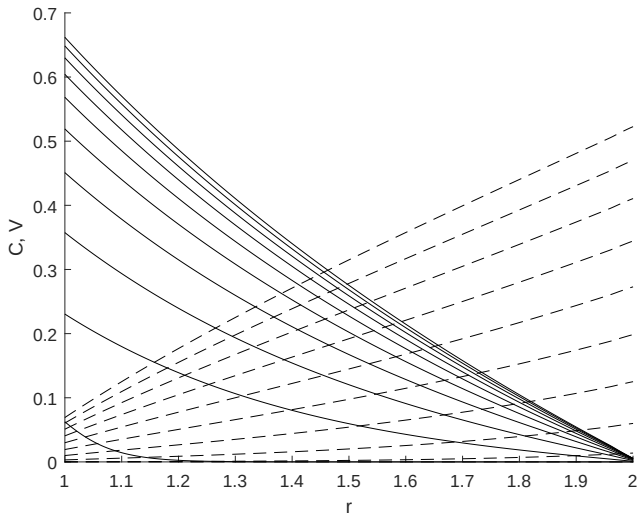

Figure 7: The distribution of nondimensionalised siderophores C (solid lines) and siderophore-iron complexes V (dashed lines) from equation (2.1) vary over the distance r from the centre of the domain and the densities increase over time. Except for key parameters described in text, parameter values are given in Table 2 and the distributions are shown at times $t = 0, 0.2, 0.4, \ldots, 2$.

3.1.3 Dependence on parameter values

Having demonstrated the agreement between the numerical solution of the full set of PDEs (2.1) and the reduced versions (3.8) with boundary conditions (3.9), the algebraic solutions of the reduced equations can be used to obtain useful predictions on the temporal behaviour of the siderophore-iron interactions. While the ultimate effect of the parameters on the final steady state distribution of the siderophores and the complexes are obvious through equation (3.12), their involvement in the time taken to reach their stationary distributions is less clear. To illustrate the delay in approaching the equilibrium distributions $C_S(r)$ and $V_S(r)$, consider the normalized functions

$$Q_C(t) = \frac{\int_1^R rC(r,t)\,\mathrm{d}r}{\int_1^R rC_S(r)\,\mathrm{d}r}, \qquad Q_V(t) = \frac{\int_1^R rV(r,t)\,\mathrm{d}r}{\int_1^R rV_S(r)\,\mathrm{d}r}, \tag{3.13}$$

which at time $t = 0$ take a value of 0 and approach 1 as the respective distributions approach their equilibria, and therefore represent the ratios of the total

amount of each population to their final amount. Notice that both numerators and denominators of (3.13) can be calculated using integration by parts.

Fig. 8 illustrates the convergence of the siderophore and siderophore-iron complex to their equilibrium distributions for different values of D. In all cases, the siderophore distribution approaches its equilibria in advance of the siderophore-iron complex. As D increases, the siderophore distribution approaches its equilibrium more rapidly, consistent with the corresponding increase in movement rates for that population. The delay between the siderophore and complex distributions approaching their equilibria increases with D up to a limiting value. For $D \ll 1$, there is a noticeable lag period before $Q_V(t)$ increases, corresponding to the time taken for the siderophores to reach the $r = R$ boundary and initiate the formation of the siderophore-iron complexes; when $D \gg 1$ no such lag is present due to the comparative reduction in transit time between the two boundaries.

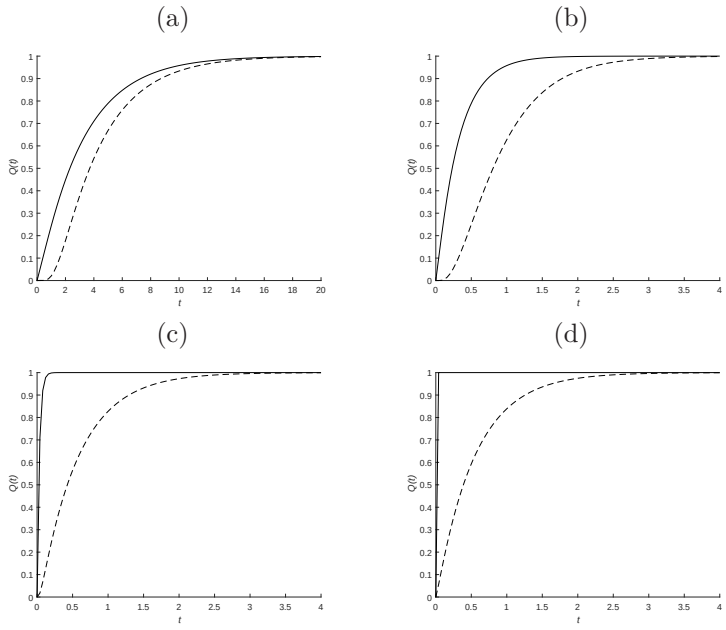

Figure 8: The functions $Q_C(t)$ (solid) and $Q_V(t)$ (dashed) with $R = 2$ are shown for (a) $D = 0.1$, (b) $D = 1$, (c) $D = 10$ and (d) $D = 100$. Note the different time scale in (a).

For large values of D, $Q_C(t)$ very quickly approaches its equilibrium value of unity so that $C(r, t)$ can be approximated by its steady state distribution $C_S(r)$ while an asymptotic expression can be constructed for the distribution $V(r, t)$ by taking leading order terms so that

$$V \approx \ln(r) + E_1\omega_1(r)e^{-\mu_1 t}.$$

Consequently for large D, by noting $r\omega_1(r) = -\frac{1}{\mu_1}(r\omega_1')'$ and using integration by parts it follows that

$$Q_V(t) \approx 1 - \frac{4E_1 e^{-\mu_1 t}\left[R\omega_1'(R) - \omega_1'(1)\right]}{\mu_1\left[1 - R^2 + 2R^2\ln R\right]}$$

and therefore the approximate time $\hat{t}$ for $Q_V(t)$ to obtain a value $\hat{Q}$ for large D is given by

$$\hat{t} = \frac{1}{\mu_1}\ln\left(\frac{4E_1\left[R\omega_1'(R) - \omega_1'(1)\right]}{\left(1-\hat{Q}\right)\mu_1\left(1 - R^2 + 2R^2\ln R\right)}\right). \tag{3.14}$$

Notice that the coefficient E_1 involves a summation of terms including λ_n. However, the asymptotic approximation in equation (3.14) where the coefficient E_1 has been truncated to only the leading term involving λ_1 agrees well with solutions obtained by algebraically solving equation (3.10) with the first 10 eigenvalues of both λ_n and μ_n using Matlab and their differences reduce with increasing D (Fig. 9).

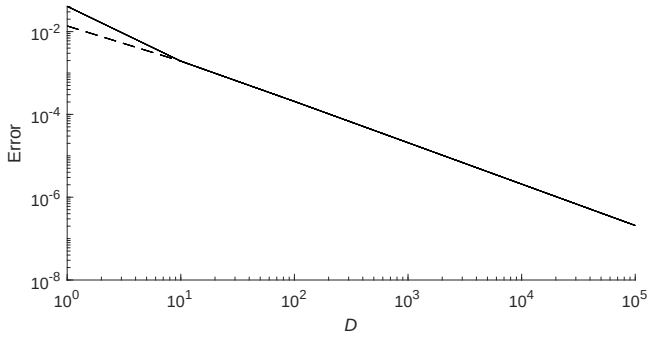

Figure 9: Absolute differences in the times taken by $Q_v(r,t)$ to approach $\hat{Q} = 0.9$ (solid) and $\hat{Q} = 0.99$ (dashed) obtained using equation (3.10) with numerically computed eigenvalues λ_n, μ_n for $n = 1, \ldots 10$ and approximation (3.14) using only μ_1 and λ_1 with $R = 2$ for different values of D.

Variations in the domain size R altered the convergence times of the distributions $Q_c(t)$ and $Q_v(t)$ to their equilibrium values (Fig. 10). The convergence times for $Q_c(t)$ and $Q_v(t)$, at least for large R, can be approximated from the corresponding leading eigenvalues, i.e. are given by $1/\sqrt{\lambda_1}$ and $1/\sqrt{\mu_1}$ respectively. Expansions for λ_1 and μ_1 are detailed below (Section 3.3) and consequently the convergence times for $Q_c(t)$ and $Q_v(t)$ scale with R and $R\sqrt{\ln R}$ respectively.

3.2 Approximations of eigenvalues λ_n and μ_n

The previous algebraic results required the numerical computation of the eigenvalues λ_n and μ_n from equations (3.11). A number of authors have constructed

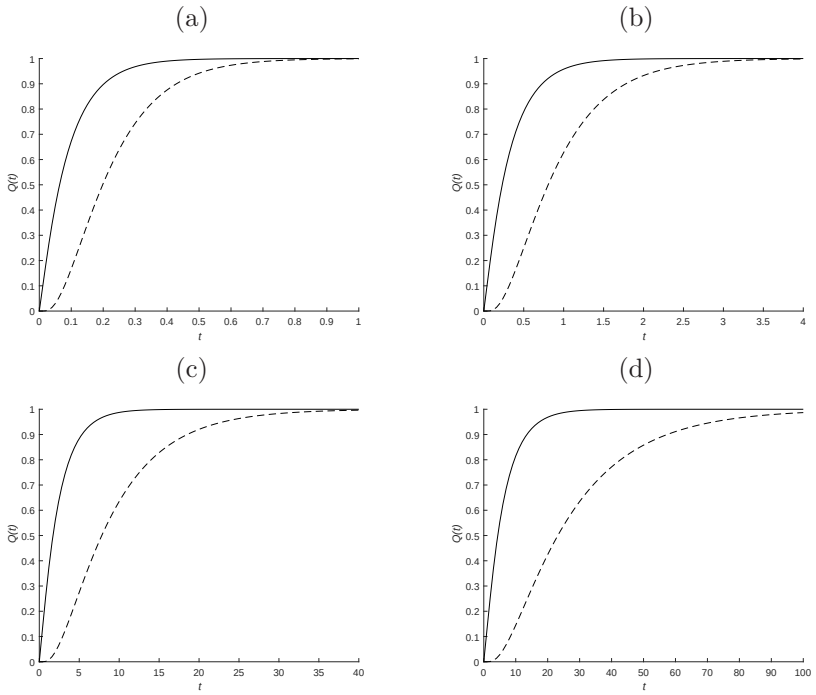

Figure 10: $Q_c(t)$ (solid) and $Q_v(t)$ (dashed) with $D = 1$ are shown for domain sizes (a) $R = 1.5$, (b) $R = 2$, (c) $R = 3$ and (d) $R = 6$.

algebraic approximations of various Bessel functions (e.g. Bowman, 2003) but these do not immediately help deduce the roots of (3.11) and hence the required eigenvalues. However, by taking an asymptotic series expansion (see Appendix B), approximations to the eigenvalues can be made resulting in an entirely algebraic solution for equation (3.10) under appropriate limits. Indeed, by defining

$$P_n(p,q) = \left| \frac{\pi(n-\frac{1}{2})}{q-p} \right|,$$

$$Q_1(p,q) = \frac{p+3q}{8pq(q-p)},$$

$$Q_3(p,q) = \frac{25p^4 - 31p^3q - 36p^2q^2 + 9pq^3 - 63q^4}{384(q-p)^2q^3p^3},$$

$$Q_5(p,q) = \frac{3219p^7 - 6938p^6q + 2279p^5q^2 + 2040p^4q^3 + 360p^3q^4 + 4797p^2q^5 - 7614pq^6 + 5697q^7}{15360p^5q^5(q-p)^3},$$

and provided $n \gg R$, the square roots of the eigenvalues for large values of R can conveniently be expressed as the series

$$\begin{aligned}\sqrt{\lambda_n} &= P_n(1,R) + \frac{Q_1(1,R)}{P_n(1,R)} + \frac{Q_3(1,R)}{P_n^3(1,R)} + \frac{Q_5(1,R)}{P_n^5(1,R)} + \cdots \\ \sqrt{\mu_n} &= P_n(R,1) + \frac{Q_1(R,1)}{P_n(R,1)} + \frac{Q_3(R,1)}{P_n^3(R,1)} + \frac{Q_5(R,1)}{P_n^5(R,1)} + \cdots\end{aligned} \tag{3.15}$$

By defining the zeroth order approximation as comprising only the first term in the series, the first order approximation comprising only the first two terms and so on, even second order approximations are in close agreement with numerically computed values for all but the smallest eigenvalues λ_1 and μ_1 for $R = 2$ (Table 3). Indeed, good approximations for the eigenvalues λ_1 and μ_1 arise provided sufficient terms in the series approximation are included. Notice, however, that in order to use these approximations it is necessary that $D \neq \mu_n/\lambda_m$ for all n, m to ensure that E_n is defined. Thus, for example, the zeroth order approximation cannot be used for $D = 1$ (but the first and higher order approximations can still be used).

	n	Numerical	0th	1st	2nd	3rd
	1	**1.7940**	1.5708	1.8493	1.7555	1.8440
	2	**4.8021**	4.7124	4.8052	4.8018	4.8021
$\sqrt{\lambda_n}$	3	**7.9090**	7.8540	7.9097	7.9089	7.9090
	4	**11.0351**	10.9956	11.0354	11.0351	11.0351
	$\vdots$					
	1	**1.3608**	1.5708	1.3719	1.3687	1.3504
	2	**4.6459**	4.7124	4.6461	4.6460	4.6459
$\sqrt{\mu_n}$	3	**7.8142**	7.8540	7.8142	7.8142	7.8142
	4	**10.9671**	10.9956	10.9672	10.9671	10.9671
	$\vdots$					

Table 3: Comparison of numerical and analytical values of eigenvalues with $R = 2$ using the approximations in equation (3.15) of stated order.

When used in (3.10), approximations (3.15) produce results consistent with the full algebraic solutions and are in strong qualitative agreement for small R (Fig. 11), especially at larger times. Such a result is unsurprising since the approximations in (3.15) were derived from asymptotic expansions of $J_\nu(z)$ and $Y_\nu(z)$ for large z and hence are most applicable for the calculation of λ_n and μ_n for large n (see also Table 3) but the smallest eigenvalues λ_1 and μ_1 exert the greatest influence on the solutions in equation (3.10), particularly at small times.

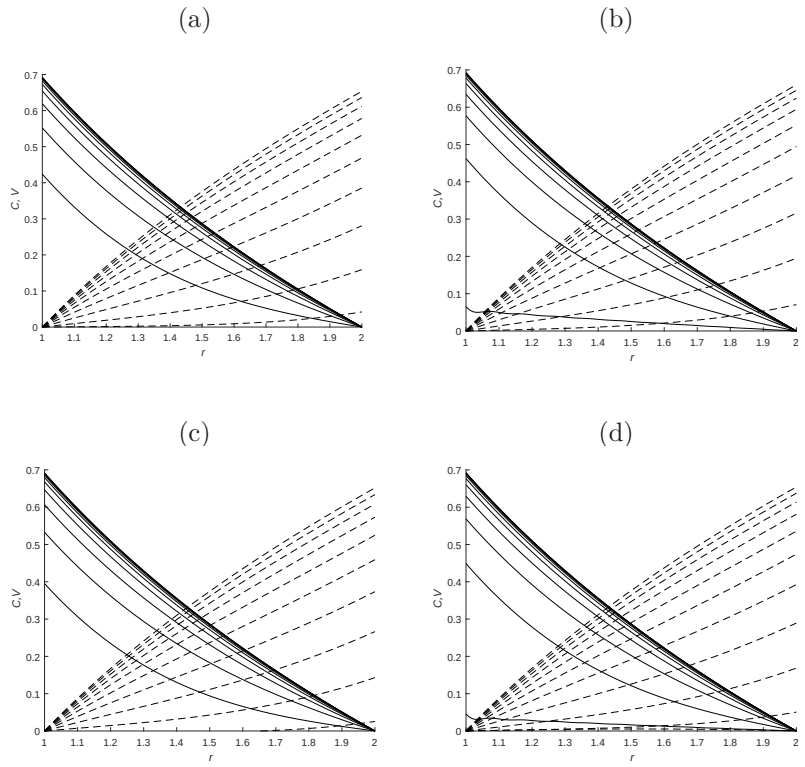

Figure 11: (a) Solution of equation (3.10) with $R = 2$, $D = 1$ using the eigenvalues computed from equation (3.11); (b), (c) and (d) using the first, second and third approximations from equation (3.15). Profiles of the siderophore distribution C (solid lines) and the siderophore-iron complex V (dashed lines) are shown at times $t = 0, 0.2, 0.4, \ldots 2$.

3.3 Approximations of leading eigenvalues λ_1 and μ_1

It was shown above that the approximations (3.15) for λ_n and μ_n are least suited for small values of n, especially $n = 1$, and also are less suited for large values of R (see Appendix B). However, the first eigenvalues λ_1 and μ_1 have the most prominent roles in the convergence of the siderophore and siderophore-iron complex to their final steady state distributions. Hence an alternative approach to approximating λ_1 and μ_1 is developed here.

By observing the behaviour of $R\sqrt{\lambda_n}$ as $R \to \infty$ it follows that (see Appendix C)

$$\sqrt{\lambda_1} = \frac{\zeta_1}{R} - \frac{\pi\zeta_1^2 Y_0(\zeta_1)}{4R^3 J_0'(\zeta_1)} + O\left(R^{-5}\ln(R)\right), \tag{3.16}$$

where ζ_1 is the first root of $J_0(\zeta) = 0$ and is valid for $\zeta_1 \ll R$. In a similar way

by considering $R\sqrt{\mu_n}$ as $R \to \infty$ (Appendix C)

$$\mu_1 = \frac{1}{R^2 \ln(R)} \left[2 + \frac{3}{2\ln(R)} + \frac{5}{6\ln(R)^2} + O\left(\frac{1}{\ln(R)^3} \right) \right], \tag{3.17}$$

which is valid provided $e \ll R$. Furthermore, related expressions can be derived for all λ_n and μ_m (Appendix C). Table 4 demonstrates that the eigenvalues λ_1 and μ_1 obtained using approximations (3.16) and (3.17) converge to those obtained using the full characteristic equations (3.11) as R increases.

	R	λ_1	μ_1	$\bar{t}$ or $\hat{t}$	t_C	t_{Cf}
Full solution	2	3.2185	1.8517	1.7783	0.3101	0.3118
from (3.11)	6	0.1768	0.0476	57.4074	6.1772	6.2190
	20	0.0146	0.0022	1170.4852	78.0076	78.6103
Approx. solutions	2	3.0979	2.1274	1.6872	0.3225	0.3242
using λ_1 and μ_1	6	0.1776	0.0480	57.1043	6.1651	6.2066
from (3.16) and (3.17)	20	0.0146	0.0022	1177.7715	78.3036	78.9064

Table 4: Solutions using numerically computed eigenvalues in equation (3.11) are compared to truncating the series to terms in only λ_1 and μ_1 from equations (3.16) and (3.17) for different domain sizes with $D = 1$. For equations (3.11), $\bar{t}$ denotes the time taken for $Q_V(\bar{t}) = 0.9$ while the approximation $\hat{t}$ is obtained from equation (3.14) using eigenvalues (3.16,3.17). t_C and t_{Cf} denote the approximate times for the siderophore concentration at $r = 1 + 0.9(R-1)$ and the flux at $r = R$ to reach half the steady state values respectively (see text for details).

These approximations for the leading eigenvalues can also be used with the normalized function $Q_V(t)$ in equation (3.13) to estimate the time taken by the siderophore-iron complex to approach its steady state distribution. Table 4 compares the numerically computed time $\bar{t}$ such that $Q_V(\bar{t}) = 0.9$ using the eigenvalues from the solutions of equation (3.11) to the approximation in equation (3.14) for $\hat{t}$ where the summation used in E_1 is restricted to its leading term, i.e. that involving only λ_1.

The approximations of λ_1 and μ_1 obtained above also allow the derivation of simple expressions relating to the spread of siderophores and the resultant uptake of iron at the $r = R$ boundary. In particular, by truncating the series to terms only involving λ_1 and μ_1 in the solutions for $C(r,t)$ in equation (3.10), the approximate time taken t_C for the siderophore density to reach a concentration $C^\dagger$ at $r = r^\dagger$ (where $1 < r^\dagger < R$ and $0 < C^\dagger < C_S(r^\dagger)$) can be shown to satisfy

$$t_C = -\frac{1}{\lambda_1 D} \ln\left(\frac{DC^\dagger - \ln(R/r^\dagger)}{A_1 D \phi_1(r^\dagger)} \right) \tag{3.18}$$

while the flux of the siderophores at the boundary $r = R$ corresponds to the acquisition of iron by the siderophores and the approximate time taken t_{Cf} for

this rate to reach a value $C_r^\dagger$ (where $0 > C_r^\dagger > -(RD)^{-1}$, representing the value at equilibrium) satisfies

$$t_{Cf} = -\frac{1}{\lambda_1 D} \ln\left(\frac{RDC_r^\dagger + 1}{RDA_1\phi_1'(R)}\right). \tag{3.19}$$

These expressions clearly illustrate the effect of the diffusion coefficient D and the radius R on the delay until the iron begins to be acquired by the siderophores. In Table 4 the approximations in equations (3.18) and (3.19) using the approximated eigenvalues (3.16) and (3.17) are compared to the corresponding algebraic solutions from equation (3.10) with numerically computed eigenvalues from equation (3.11). The simple approximations using (3.16) and (3.17) are in strong qualitative and quantitative agreement with the full algebraic solution and the agreement improves as R is increased due to two independent reasons; firstly the approximation of the leading eigenvalues improves as $R \to \infty$ and, secondly, as R increases, it takes longer for the siderophores to reach the exterior boundary at $r = R$ and hence the second and higher eigenvalues play less significant roles in determining the distributions of $C(r, t)$ and $V(r, t)$.

4 Discussion

Siderophores play a central role in how microorganisms acquire important elements. While there are known to be hundreds of different types of siderophores with various functionalities, the most studied relationship is that with iron and thus the subject of this investigation. Indeed, it has recently been shown that siderophores significantly increase the rate at which bacteria acquire this important resource compared to alternative methods (Niehus et al., 2017; Leventhal et al., 2019).

Equation (2.1) represents, to the authors' knowledge, the first mathematical model of iron uptake in fungi mediated through siderophores. The numerical simulations of the model equations display the same qualitative features observed in experiments regarding the extraction of iron from a solid growth medium; specifically there is a radially-symmetric depletion of the iron that extends beyond the edge of the expanding biomass (Fig. 1) and that this region expands initially in an approximately linear fashion at rates determined by local conditions (Figs. 2 & 3). In limiting conditions, e.g. Fig. 3(a), the expansion of the siderophore distribution and the concomitant depletion of the iron concentration was clearly less than linear and instead the extent of the iron depletion appeared to increase with the square root of time, consistent with the reduced production and diffusive movement properties of the siderophores. A key feature of the model was its ability to predict the cumulative amount of iron taken up by the biomass through the absorption of the iron-siderophore complexes, as represented by equation (2.3). Such time-dependent data is difficult to obtain experimentally through either direct or indirect means as destructive sampling of the biomass provides the most accurate measurements of the former while the latter is limited since there is currently no convenient procedure to

measure siderophore populations given their diversity. Nonetheless, our model clearly has the potential to make such quantitative predictions on iron acquisition by mycelial fungi. Moreover, further refinements should account for such siderophore-diversity and the different pathways through which iron is utilized by fungi following its acquisition (e.g. Howard, 1999). It should also be noted that the model equations represent a simplification of how a combination of different nutrients can impact on the growth and function of a fungal mycelium through the merger of internalised iron and the generic substrate. While alternative approaches have been used to model how fungi utilize combinations of nutrients and essential elements (e.g. Lamour et al., 2000), due to the generalized treatment of the iron pathway once that substance was internalised by the fungus, the precise role of iron on key morphological processes was not isolated in this current study and therefore remains an important avenue for future investigations which would necessitate the inclusion of feedback processes by restricting siderophore production to prevent excessive accumulation of iron.

Key features of the numerical solution of the full set of equations (2.1) were captured in the algebraic solutions of the reduced set of equations (3.8), including the constant uptake rate of iron for all but small times. Indeed, there was strong qualitative and quantitative agreement between the full numerical solutions and the algebraic simplifications in the distributions of siderophores and siderophore-iron complexes (Figs. 6 & 7). The nondimensionalisation used to construct the algebraic solutions (3.10) introduced the parameter D representing the ratio of the diffusion coefficients of the siderophores and the siderophore-iron complexes. Since the diffusion coefficient of the complexes is less than that of the siderophores (due to obvious differences in their molecular weight), it follows in application that $D > 1$ and therefore siderophores are released and complexes are formed more rapidly than they are acquired by the biomass until equilibrium is reached (Fig. 8). Consequently, equation (3.14) with $\hat{Q} = 0.9$ (or 0.99) is expected to provide a reasonable estimate for the time taken for the siderophore-iron complex distribution to approach its equilibria. The same algebraic solutions also demonstrated the impact of domain size on siderophore and siderophore-iron complex distribution. Specifically, greater distances between the biomass and the source of iron resulted in greater concentrations of both populations (equation (3.12)).

An important consequence of the model equations is the ability to calculate the cumulative amount of iron taken up by the biomass through the release of siderophores and the subsequent acquisition of the siderophore-iron complexes. Other than during an initial transient period, the total uptake rate of iron was approximately linear (Fig. 4) except when influenced by boundary effects. Indeed, this same qualitative feature is captured in the reduced model in Section 3 by observing that for large D (i.e. when $D_c \gg D_v$) the uptake of iron corresponded to the flux of the complex at $r = 1$ which to leading order from

equation (3.10) is given by

$$\left.\frac{\partial V}{\partial r}\right|_{r=1} \approx 1 + E_1\omega_1'(1)e^{-\mu_1 t}$$

and tends to the constant unity. However, this rate was heavily influenced by local conditions. While an increased concentration of external substrate resulted in an increase of iron extracted from the growth domain and internalized by the biomass, the relationship was highly nonlinear; a ten-fold increase in external substrate only approximately doubled the amount of iron obtained by the biomass. However, the observation that external resources can influence the depletion of iron from the growth environment clearly has important consequences in the bio-technological applications of fungi.

While the algebraic results presented in this paper have focussed on radial geometry, similar treatments are possible in other domains including a single-dimension Cartesian and spherical radial geometries. (Indeed, by introducing x so that $r = R_1 + (R_2 - R_1)x$ and letting $R_2 - R_1 \to \infty$, equations (3.1) and (3.5) can be easily converted into a one-dimensional Cartesian geometry with spatial coordinate x resulting in Fourier series solutions for the siderophore and complex populations. Such a situation has been thoroughly explored in Choudhury (2019).) In our calculations, the algebraic solutions (3.10) are defined provided the nondimensionalised diffusion coefficient D is not a ratio of the eigenvalues λ_n and μ_m for all n, m. In one-dimensional Cartesian geometry, the equivalent restriction corresponds to D not being a ratio of squares of odd numbers (however, alternative solutions can be constructed by selecting an alternative form for $\hat{V}$ in Appendix A, equation (A.15)). Moreover, similar issues arise in the spherical radial geometry case. We cannot provide any physical reasoning behind this limitation. Further interesting analysis would concern the implementation of moving boundary conditions consistent with the depletion of the iron concentration and the advancement of the fungal biomass. Such a situation would more closely represent the scenarios considered in Section 2.

Siderophores are extensively used by microorganisms to obtain essential metals, in particular iron. In this work we have constructed and investigated the first mathematical model of their use by fungi. The qualitative behaviour of the model is consistent with known experiments and quantitative predictions have been made on how local conditions influence the amount of iron obtained by the fungus along with how key distributions involving siderophore function change over time. It remains to develop a suitable experimental technique to verify these predictions. We note that the model does not consider how the fungus subsequently uses the iron it has obtained and this is therefore an important challenge for future modelling investigations.

References

Ahmed, E. and S. J. M. Holmström (2014). Siderophores in environmental research: roles and applications. *Microbial Biotechnology 7*3, 196–208.

747 Andrews, M. Y., C. M. Santelli, and O. W. Duckworth (2016a). Digital image
748 quantification of siderophores on agar plates. *Data in Brief 6*, 890–898.

749 Andrews, M. Y., C. M. Santelli, and O. W. Duckworth (2016b). Layer plate CAS
750 assay for the quantification of siderophore production and determination of
751 exudation patterns for fungi. *Journal of Microbiological Methods 121*, 41–43.

752 Beard, J. L. (2008). Why iron deficiency is important in infant development.
753 *Journal of Nutrition 138*, 2534–2536.

754 Bellenger, J. P., T. Wichard, A. B. Kustka, and A. M. L. Kraepiel (2013).
755 Uptake of molybdenum and vanadium by a nitrogen-fixing soil bacterium
756 using siderophores. *Nature Geoscience 1*, 243–246.

757 Ben-Haim, E. and S. Redner (1992). Inhomogeneous two-species annihilation
758 in the steady state. *Journal of Physics A: Mathematical and General 25*,
759 575–583.

760 Bertrand, S., J. P. Bouchara, M. C. Venier, P. Richomme, O. Duval, and
761 G. Larcher (2010). N^{α}-methyl coprogen B, a potential marker of the airway
762 colonization by *Scedosporium apiospermum* in patients with cystic fibrosis.
763 *Medical Mycology 48 Suppl 1*, S98–107.

764 Bogumił, A., L. S. Paszt, A. Lisek, P. Trzciński, and A. Harbuzov (2013). Identi-
765 fication of new *Trichoderma* strains with antagonistic activity against *Botrytis*
766 *cinerea*. *Folia Horticulturae 25*, 123–132.

767 Boswell, G. P., H. Jacobs, F. A. Davidson, G. M. Gadd, and K. Ritz (2002).
768 Functional consequences of nutrient translocation in mycelial fungi. *Journal*
769 *of Theoretical Biology 217*, 459–477.

770 Boswell, G. P., H. Jacobs, F. A. Davidson, G. M. Gadd, and K. Ritz (2003).
771 Growth and function of fungal mycelia in heterogeneous environments. *Bul-*
772 *letin of Mathematical Biology 65*, 447–477.

773 Boswell, G. P., H. Jacobs, K. Ritz, G. M. Gadd, and F. A. Davidson (2007).
774 The development of fungal networks in complex environments. *Bulletin of*
775 *Mathematical Biology 69*, 605–634.

776 Boukhalfa, H., J. Lack, S. D. Reilly, L. Herman, and M. P. Neu (2003).
777 Siderophore production and facilitated uptake of iron and plutonium in *P.*
778 *putida*. *AIP Conference Proceedings 673*, 343–344.

779 Bowman, F. (2003). *Introduction to Bessel functions*. Dover.

780 Braud, A., F. Hoegy, K. Jezequel, T. Lebeau, and I. J. Schalk (2009). New
781 insights into the metal specificity of the *Pseudomonas aeruginosa* pyoverdine-
782 iron uptake pathway. *Environmental Microbiology 11*, 1079–1091.

783 Choudhury, M. J. A. (2019). *Mathematical modelling of fungal interactions*. Ph.
784 D. thesis, University of South Wales.

Choudhury, M. J. A., P. M. J. Trevelyan, and G. P. Boswell (2018). A mathematical model of nutrient influence on fungal competition. *Journal of Theoretical Biology 438*, 9–20.

Eberi, H. J. and S. Collinson (2009). A modelling and simulation study of siderophore mediated antagonism in dual-species biofilms. *Theoretical Biology and Medical Modelling 6*(30), 1–16.

Fettis, H. E. and J. C. Caslin (1966). *An extended table of zeros of cross products of Bessel functions*. Report No. ARL 66-0023, Aerospace Research Laboratories, Office of Aerospace Research, United States Air Force, Wright-Patterson Air Force Base, Ohio.

Fomina, M., K. Ritz, and G. M. Gadd (2000). Negative fungal chemotropism to toxic metals. *FEMS Microbiology Letters 193*, 207–211.

Ghosh, S., S. Pal, and N. Chakraborty (2015). The qualitative and quantitative assay of siderophore production by some microorganism and effects of different media on tis production. *International Journal of Chemical Science 13*, 1621–1629.

Gruhn, C. M., A. Gruhn, and O. K. Miller (1992). *Boletinellus meruliodes* alter root morphology of *pinus densiflora* without mycorrhizal formation. *Mycologia 84*, 528–533.

Haas, H. (2014). Fungal siderophore metabolism with a focus on *Aspergillus fumigatus*. *Natural Product Reports 31*, 1266–1276.

Harrison, J. (2009). Fast and accurate Bessel function computation. In *Proceedings of the 2009 19th IEEE Symposium on Computer Arithmetic*, pp. 104–113. Washington DC: IEEE Computer Society.

Howard, D. H. (1999). Acquisition, transport, and storage of iron by pathogenic fungi. *Clinical Micriobiology Review 12*, 394–404.

Johnson, L. (2008). Iron and siderophores in fungal-host interactions. *Mycological Research 112*, 170–183.

Kraemer, S. M., A. Butler, P. Borer, and J. Cervini-Silva (2005). Siderophores and the dissolution of iron-bearing minerals in marine systems. *Reviews in Mineralogy and Geochemistry 59*, 53–84.

Lamour, A., F. van den Bosch, and A. J. T. amd M. J. Jeger (2000). Modelling the growth of soil-borne fungi in response to carbon and nitrogen. *Mathematical Medicine and Biology 17*, 329–346.

Leventhal, G. E., M. Ackermann, and K. T. Schiessl (2019). Why microbes secrete molecules to modify their environment: the case of iron-chelating siderophores. *Journal of the Royal Society Interface 16*(150), 20180674.

Machuca, A. and A. M. F. Milagres (2003). Use of CAS-agar plate modified to study the effect of different variables on the siderophore production by *aspergillus*. *Letters in Applied Microbiology 36*, 177–181.

Marschner, H. (1995). *Mineral nutrition of higher plants*. Academic Press.

McLoughin, T. J., J. P. Quinn, A. Bettermann, and R. Bookland (1992). *Pseudomonas cepacia* suppression of sunflower wilt fungus and role of antifungal compounds in controlling the disease. *Applied Environmental Microbiology 58*, 1760–1763.

Milagres, A. M. F., A. Machuca, and D. Napoleão (1999). Detection of siderophore production from several fungi and bacteria by a modification of chrome Azurol S (CAS) agar plate assay. *J. Microbiol. Methods 37*, 1–6.

Niehus, R., A. Picot, N. M. Oliveira, S. Mitri, and K. R. Foster (2017). The evolution of siderophore production as a competitive trait. *Evolution: International Journal of Organic Evolution 71*, 1443–1455.

Perez-Meranda, S., N. Cabirol, R. George-Tellez, L. S. Zamudio-Rivera, and F. J. Fernandez (2007). O-CAS, a fast universal method for siderophore detection. *Journal of Microbiolgical Methods 70*, 127–131.

Philpott, C. C., S. Leidgens, and A. G. Frey (2012). Metabolic remodeling in iron-deficient fungi. *Biochimica et Biophysica Acta (BBA) - Molecular Cell Research 1823*, 1509–1520.

Prosser, J. I. and A. P. J. Trinci (1979). A model for hyphal growth and branching. *Journal of General Microbiology 111*, 153–164.

Renshaw, J. C., G. D. Robson, A. P. J. Trinci, M. Wiebe, F. R. Livens, D. Collison, and R. J. Taylor (2002). Fungal siderophores: structures, functions and applications. *Mycological Research 106*, 1123–1142.

Riquelme, M., J. Aguirre, S. Bartnicki-García, G. H. Braus, M. Feldbrügge, U. Fleig, W. Hansberg, A. Herrar-Estrella, J. Kämper, U. Kück, R. R. Mouriño-Pérez, N. Takeshita, and R. Fischer (2018). Fungal morphogenesis, from the polarized growth of hyphae to complex reproduction and infection structures. *Microbiology and Molecular Biology Reviews 82*, e00068–17.

Saha, M., S. Sarkar, B. Sarkar, B. K. Sharma, S. Bhattacharjee, and P. Tribedi (2016). Microbial siderophores and their potential: a review. *Environmental Science and Pollution Research International 23*, 3984–2999.

Sasirekha, B. and S. Srividya (2016). Siderophore production by *Pseudomonas aeruginosa FP6*, a biocontrol strain for *Rhizoctonia solani* and *Colletotrichum gloesporioides* causing diseases in chilli. *Agriculture and Natural Resources 50*, 250–256.

Schwyn, B. and J. B. Neilands (1987). Universal chemical assay for the detection and determination of siderophores. *Analytical Biochemistry 160*, 47–56.

Srivastava, M. P., R. Tiwari, and N. Sharma (2013). Effect of different cultural variables on siderophores produced by *Trichoderma spp. International Journal of Advanced Research 1*, 1–6.

Suberkropp, K. (2011). The influence of nutrients on fungal growth, productivity, and sporulation during leaf breakdown in streams. *Canadian Journal of Botony 73*, 1361–1369.

Van der Helm, D. and G. Winkelmann (1994). Hydroxamates and polycarboxylates as iron transport agents (siderophores) in fungi. In G. Winkelmann and D. Winge (Eds.), *Metal Ions in Fungi*. Marcel Dekker.

Verma, V. C., S. K. Singh, and S. Prakash (2011). Bio-control and plant growth promotion potential of siderophore producing endophytic streptomyces from *Azadirachta indica A. Juss. Journal of Basic Microbiology 51*, 550–556.

Winkelmann, G. (1991). Structural and stereochemical aspects of iron transport in fungi. *Biotechnology Advances 8*, 207–231.

Winkelmann, G. (2002). Microbial siderophores-mediated transport. *Biochemical Society Transactions 30*, 691–695.

Winkelmann, G. (2007). Ecology of siderophores with specia reference to the fungi. *Biometals 20*, 379–392.

Zimmermann, M. B. and R. F. Hurrell (2007). Nutritional iron deficiency. *Lancet 370*, 511–520.

A Solution of equation (3.8)

Here we consider the model equations

$$\frac{\partial C}{\partial t} = \frac{D}{r}\frac{\partial}{\partial r}\left(r\frac{\partial C}{\partial r}\right), \tag{A.1a}$$

$$\frac{\partial V}{\partial t} = \frac{1}{r}\frac{\partial}{\partial r}\left(r\frac{\partial V}{\partial r}\right), \tag{A.1b}$$

for $1 < r < R$ with boundary conditions and initial data

$$D\frac{\partial C}{\partial r}(1,t) = -1, \qquad V(1,t) = 0, \tag{A.2a}$$

$$C(R,t) = 0, \qquad D\frac{\partial C}{\partial r}(R,t) = -\frac{\partial V}{\partial r}(R,t), \tag{A.2b}$$

$$C(r,0) = V(r,0) = 0. \tag{A.2c}$$

Due to the boundary conditions (A.2b), we first solve equation (A.1a) and then construct the solution for equation (A.1b).

A.1 Solution of (A.1a)

From the non-homogeneous boundary conditions in equation (A.2), we suppose that $C(r,t) = C_S(r) + \hat{C}(r,t)$ where $C_S(r)$ denotes the steady-state distribution and satisfies those same non-homogeneous boundary conditions while $\hat{C}(r,t)$ satisfies homogeneous boundary conditions (and therefore represents the transition of the initial data (A.2c) towards the final steady state distribution $C_S(r)$).

The steady state distribution $C_S(r)$ satisfies

$$0 = \frac{\mathrm{d}}{\mathrm{d}r}\left(r\frac{\mathrm{d}C_S}{\mathrm{d}r}\right), \qquad \text{for } 1 < r < R.$$

After integrating twice and applying the non-homogeneous boundary conditions (A.2), the corresponding steady state solution is given by

$$C_S(r) = \frac{1}{D}\ln\left(\frac{R}{r}\right). \tag{A.3}$$

The function $\hat{C}(r,t)$ satisfies equation (A.1a) but the corresponding boundary conditions (A.2a) and (A.2b) are expressed as

$$\frac{\partial \hat{C}}{\partial r}(1,t) = 0, \qquad \hat{C}(R,t) = 0, \tag{A.4}$$

while the corresponding initial data is

$$\hat{C}(r,0) = -C_S(r). \tag{A.5}$$

By assuming $\hat{C}(r,t) = \hat{F}(r)\hat{G}(t)$, separating variables yields

$$\hat{G}(t) = e^{-\lambda D t} \tag{A.6}$$

and the Bessel differential equation $r\hat{F}'' + \hat{F}' + r\lambda\hat{F} = 0$ (where $'$ denotes differentiation with respect to r), which has general solution

$$\hat{F} = c_1 J_0\left(\sqrt{\lambda}r\right) + c_2 Y_0\left(\sqrt{\lambda}r\right) \tag{A.7}$$

where J_0 and Y_0 are the Bessel functions of first and second kind respectively. From the boundary condition at $r = R$, equation (A.4) allows the constant c_2 to be expressed in terms of c_1 and by introducing $A = c_2 Y_0(\sqrt{\lambda}R)$ and

$$\phi(r) = \frac{Y_0\left(\sqrt{\lambda}r\right)}{Y_0\left(\sqrt{\lambda}R\right)} - \frac{J_0\left(\sqrt{\lambda}r\right)}{J_0\left(\sqrt{\lambda}R\right)}, \tag{A.8}$$

it follows that

$$\hat{F}(r) = A\phi(r). \tag{A.9}$$

Substituting equations (A.6) and (A.9) into the boundary condition on $r = 1$ yields the characteristic equation

$$\frac{J_1\left(\sqrt{\lambda}\right)}{J_0\left(\sqrt{\lambda}R\right)} - \frac{Y_1\left(\sqrt{\lambda}\right)}{Y_0\left(\sqrt{\lambda}R\right)} = 0, \tag{A.10}$$

with roots λ_n denoting the eigenvalues. Thus $\hat{C}(r,t)$ can be represented by the series

$$\hat{C}(r,t) = \sum_{n=1}^{\infty} A_n \phi_n(r) e^{-\lambda_n D t}, \qquad \text{for } 1 < r < R \tag{A.11}$$

where A_n are constants and the eigenfunctions $\phi_n(r)$ are obtained from equation (A.8) evaluated with $\lambda = \lambda_n$. Notice that $\phi_n(R) = 0$, $\phi_n'(1) = 0$ and $r\phi_n'' + \phi_n' + \lambda_n r \phi_n = 0$.

From equation (A.5) there is a generalized Fourier series satisfying

$$\frac{1}{D}\ln\left(\frac{r}{R}\right) = \sum_{n=1}^{\infty} A_n \phi_n(r)$$

and hence the constants A_n can be determined as

$$A_n = \frac{\int_1^R r\ln(r/R)\phi_n(r)\,\mathrm{d}r}{D\int_1^R r\phi_n(r)^2\,\mathrm{d}r}.$$

By noting that $(r\phi_n')' + \lambda_n r\phi_n = 0$, integrating by parts and recalling that $\phi_n'(1) = 0$ and $\phi_n(R) = 0$ we obtain

$$\int_1^R r\ln(r/R)\phi_n(r)\,\mathrm{d}r = -\frac{\phi_n(1)}{\lambda_n}.$$

Using a similar approach (Bowman, 2003),

$$\int_1^R r\phi_n(r)^2\,\mathrm{d}r = \frac{R^2}{2\lambda_n}\left(\phi_n'(R)\right)^2 - \frac{1}{2}\phi_n^2(1).$$

Consequently, after some simplification,

$$A_n = \frac{2\phi_n(1)}{D\left[\phi_n^2(1)\lambda_n - R^2(\phi_n'(R))^2\right]}, \tag{A.12}$$

and hence the solution of equation (A.1a) is

$$C(r,t) = \frac{1}{D}\ln\left(\frac{R}{r}\right) + \sum_{n=1}^{\infty} A_n\phi_n(r)e^{-\lambda_n D t}, \qquad \text{for } 1 < r < R \tag{A.13}$$

where A_n, λ_n and $\phi_n(r)$ are defined in (A.12), (A.10) and (A.8) respectively.

A.2 Solution of (A.1b)

Due to the boundary conditions (A.2), and in particular the flux condition on $r = R$, we seek a solution of the form $V(r,t) = V_S(r) + \bar{V}(r,t) + \hat{V}(r,t)$ where $V_S(r)$ denotes the steady state solution, $\bar{V}(r,t)$ matches the temporal change due to the relationship between the fluxes of $C(r,t)$ and $V(r,t)$ at $r = R$, and $\hat{V}(r,t)$ accounts for the change from the initial data.

The steady-state solution $V_S(r)$ satisfies the ODE

$$0 = \frac{1}{r}\frac{\mathrm{d}}{\mathrm{d}r}\left(r\frac{\mathrm{d}V_S}{\mathrm{d}r}\right), \qquad \text{for } 1 < r < R,$$

with boundary conditions $V_S(1) = 0$ and $\frac{\mathrm{d}V_S}{\mathrm{d}r}(R) = -D\frac{\mathrm{d}C_S}{\mathrm{d}r}(R)$. Consequently we see that

$$V_S(r) = \ln(r). \tag{A.14}$$

The function $\bar{V}(r,t)$ satisfies the PDE in (A.1b) but with boundary conditions

$$\bar{V}(1,t) = 0, \qquad \frac{\partial \bar{V}}{\partial r}(R,t) = -D\frac{\partial \hat{C}}{\partial r}(R,t), \tag{A.15}$$

where $\hat{C}(r,t)$ is defined in equation (A.11). Due to the form of $\hat{C}(r,t)$, suppose

$$\bar{V}(r,t) = \sum_{n=1}^{\infty} B_n \psi_n(r) e^{-\lambda_n D t} \tag{A.16}$$

for suitable constants B_n and eigenfunction $\psi_n(r)$. Since $\bar{V}(r,t)$ satisfies equation (A.1b), it follows that

$$r\psi'' + \psi_n' + \lambda_n D r \psi_n = 0$$

and hence

$$\psi_n(r) = c_3 J_0\left(\sqrt{\lambda_n D}r\right) + c_4 Y_0\left(\sqrt{\lambda_n D}r\right)$$

where c_3 and c_4 are constants. Since $\psi_n(1) = 0$ from (A.15), the constant c_3 can be expressed in terms of c_4 and by substituting into the boundary condition on $r = R$ and defining

$$\psi_n(r) = \frac{Y_0\left(\sqrt{\lambda_n D}r\right)}{Y_0\left(\sqrt{\lambda_n D}\right)} - \frac{J_0\left(\sqrt{\lambda_n D}r\right)}{J_0\left(\sqrt{\lambda_n D}\right)} \tag{A.17}$$

it follows that

$$B_n \psi_n'(R) = -D A_n \phi_n'(R) \tag{A.18}$$

and provided $\psi_n'(R) \neq 0$ the constants B_n can be evaluated. Hence

$$\bar{V}(r,t) = -D\sum_{n=1}^{\infty} A_n \frac{\phi_n'(R)}{\psi_n'(R)}\psi_n(r)e^{-\lambda_n D t}, \qquad \text{for } 1 < r < R. \tag{A.19}$$

The function $\hat{V}(r,t)$ satisfies equation (A.1b) with homogeneous boundary conditions and initial data given by

$$\hat{V}(1,t) = 0, \qquad \frac{\partial \hat{V}}{\partial r}(R,t) = 0, \qquad \hat{V}(r,0) = -V_S(r) - \bar{V}(r,0). \tag{A.20}$$

By supposing $\hat{V}(r,t) = \tilde{F}(r)\tilde{G}(t)$, separating variables and integrating gives

$$\tilde{G}(t) = e^{-\mu t}, \tag{A.21}$$

while $\tilde{F}(r)$ satisfies

$$r\tilde{F}'' + \tilde{F}' + \mu r\tilde{F} = 0.$$

As above, the general solution for $\tilde{F}(r)$ can be expressed in terms of Bessel functions while the boundary condition (A.20) on $r = 1$ gives $\tilde{F}(r) = E\omega(r)$ where E is a constant and

$$\omega(r) = \frac{Y_0(\sqrt{\mu}r)}{Y_0(\sqrt{\mu})} - \frac{J_0(\sqrt{\mu}r)}{J_0(\sqrt{\mu})}. \tag{A.22}$$

The boundary condition (A.20) on $r = R$ therefore gives the eigenvalues μ_n as the roots of

$$\frac{J_1(\sqrt{\mu}R)}{J_0(\sqrt{\mu})} - \frac{Y_1(\sqrt{\mu}R)}{Y_0(\sqrt{\mu})} = 0. \tag{A.23}$$

Hence $\hat{V}(r,t)$ is given by

$$\hat{V}(r,t) = \sum_{n=1}^{\infty} E_n \omega_n(r) e^{-\mu_n t}, \qquad \text{for } 1 < r < R, \tag{A.24}$$

where E_n are constants and $\omega_n(r)$ is equation (A.22) evaluated at $\mu = \mu_n$. Note that for all n, $\omega_n(1) = 0$, $\omega_n'(R) = 0$ and $r\omega_n'' + \omega_n' + \mu_n r\omega_n = 0$. It now only remains to determine the constants E_n. The initial data in (A.20) gives

$$-\ln(r) + D\sum_{n=1}^{\infty} A_n \frac{\phi_n'(R)}{\psi_n'(R)}\psi_n(r) = \sum_{m=1}^{\infty} E_m \omega_m(r).$$

By noting that

$$\int_1^R r\omega_n(r)\omega_m(r)\,\mathrm{d}r = 0 \text{ for all } n \neq m,$$

it follows that

$$E_m = \frac{\int_1^R r\left[-\ln(r) + D\sum_{n=1}^{\infty} A_n \frac{\phi_n'(R)}{\psi_n'(R)}\psi_n(r)\right]\omega_m(r)\,\mathrm{d}r}{\int_1^R r\omega_m^2(r)\,\mathrm{d}r}. \tag{A.25}$$

By making use of the identities noted above, integration by parts yields

$$\int_1^R r\ln(r)\omega_m(r)\,\mathrm{d}r = \frac{\omega_m(R)}{\mu_m},$$
$$\int_1^R r\omega_m^2(r)\,\mathrm{d}r = \frac{R^2}{2}\omega_m^2(R) - \frac{1}{2\mu_m}\left(\omega_m'(1)\right)^2,$$
$$\int_1^R r\psi_n(r)\omega_m(r)\,\mathrm{d}r = \frac{R\psi_n'(R)\omega_m(R)}{\mu_m - D\lambda_n},$$

provided $\mu_m \neq D\lambda_n$. By using the above integrals and after some length algebra, equation (A.25) yields

$$E_m = \frac{2\omega_m(R)\left[1 - R\mu_m D\sum_{n=1}^{\infty}\frac{A_n\phi_n'(R)}{\mu_m - D\lambda_n}\right]}{\left[\left(\omega_m'(1)\right)^2 - \mu_m R^2\omega_m^2(R)\right]}, \tag{A.26}$$

again provided $\mu_m \neq D\lambda_n$.

Finally from equations (A.14), (A.19) and (A.24) it follows that the solution of equation (A.1b) is given by

$$V(r,t) = \ln(r) - D\sum_{n=1}^{\infty} A_n\frac{\phi_n'(R)}{\psi_n'(R)}\psi_n(r)e^{-\lambda_n Dt} + \sum_{n=1}^{\infty} E_n\omega_n(r)e^{-\mu_n t}, \qquad \text{for } 1 < r < R, \tag{A.27}$$

where $\phi_n(r)$ is given in equation (A.8), $\psi_n(r)$ is given in equation (A.17), λ_n are the roots of (A.10), $\omega_n(r)$ is stated in (A.22), μ_n are the roots of (A.23) and the constants A_n and E_n are defined by equations (A.12) and (A.26) respectively.

B Derivation of approximations (3.15)

The characteristic equations (3.11) are of the form

$$J_1(xp)Y_0(xq) - J_0(xq)Y_1(xp) = 0 \tag{B.1}$$

where x denotes the square root of the eigenvalue and $p \neq q$ take either the values 1 or R (depending on which eigenvalue λ or μ is being considered). Using Hankel's asymptotic expansions, Harrison (2009) obtained approximations, valid for large values of z, for the Bessel functions

$$J_n(z) = \sqrt{\frac{2}{\pi z}}\beta_n(z)\cos\left(z - \frac{\pi}{4} - \alpha_n(z)\right),$$
$$Y_n(z) = \sqrt{\frac{2}{\pi z}}\beta_n(z)\sin\left(z - \frac{\pi}{4} - \alpha_n(z)\right),$$

for suitable series $\alpha_n(z)$ and $\beta_n(z)$ each in terms of powers of $1/z$. To determine the roots of the characteristic equation (B.1), we note from Harrison (2009) that

for $|z| \gg 1$

$$\alpha_0(z) = \frac{1}{8z} - \frac{25}{384z^3} + \frac{1073}{5120z^5} - \frac{375733}{229376z^7} + O\left(\frac{1}{z^9}\right),$$

$$\alpha_1(z) = -\frac{3}{8z} + \frac{21}{128z^3} - \frac{1899}{5120z^5} + \frac{543483}{229376z^7} + O\left(\frac{1}{z^9}\right).$$

By using these expressions in the generalised characteristic equation (B.1), it follows that

$$\sin\left((q-p)x + \frac{\pi}{2} + \alpha_1(px) - \alpha_0(qx)\right) = 0. \tag{B.2}$$

Consequently, equation (B.2) gives rise to

$$x\left[1 + \frac{\alpha_1(px) - \alpha_0(qx)}{(q-p)x}\right] = P_n(p,q) \tag{B.3}$$

where n is an integer and

$$P_n(p,q) = \frac{\pi(n-\frac{1}{2})}{q-p}.$$

Since we seek positive roots x and note that

$$\frac{\alpha_1(px) - \alpha_0(qx)}{(q-p)x} \to 0 \qquad \text{as } x \to \infty,$$

it follows that $P_n(p,q) > 0$ and so if $q > p$ then n has to be a positive integer. (The case $q < p$ is treated below.)

Equation (B.3) can therefore be written as the summation of a series of even powers of $1/x$

$$x\left[1 + \frac{a_2(p,q)}{x^2} + \frac{a_4(p,q)}{x^4} + O\left(\frac{1}{x^6}\right)\right] = P_n(p,q)$$

where the coefficients $a_n(p,q)$ are easily determined from the above series for $\alpha_0(qx)$ and $\alpha_1(px)$. By constructing the reciprocal of the series on the left it follows that

$$\frac{1}{P_n(p,q)} = \frac{1}{x} + \frac{3q+p}{8pq(q-p)x^3} + \frac{25p^4 - 19p^3q + 36p^2q^2 + 117pq^3 - 63q^4}{384p^3q^3(q-p)^2x^5}$$
$$+ \frac{3219p^7 - 6188p^6q + 3749p^5q^2 - 480p^4q^3 + 1440p^3q^4 + 7767p^2q^5 - 13284pq^6 + 5697q^7}{15360p^5q^5(q-p)^3x^7} + O\left(\frac{1}{x^9}\right).$$

By using series inversion, a power series for $\frac{1}{x}$ in terms of odd powers of $\frac{1}{P_n(p,q)}$ is obtained and is given by

$$\frac{1}{x} = \frac{1}{P_n(p,q)} - \frac{p+3q}{8pq(q-p)P_n(p,q)^3} - \frac{25p^4 - 37p^3q - 72p^2q^2 - 45pq^3 - 63q^4}{384p^3q^3(q-p)^2P_n(p,q)^5}$$
$$- \frac{1073p^7 - 2396p^6q + 623p^5q^2 + 1200p^4q^3 + 720p^3q^4 + 1989p^2q^5 - 1908pq^6 + 1899q^7}{5120p^5q^5(q-p)^3P_n(p,q)^7} + O\left(\frac{1}{P_n(p,q)^9}\right).$$

Multiplying through by $P_n(p,q)$ produces a power series for $\frac{P_n(p,q)}{x}$ in terms of even powers of $\frac{1}{P_n(p,q)}$. Taking reciprocals and then finally multiplying through by $P_n(p,q)$ yields

$$x = P_n(p,q) + \frac{Q_1(p,q)}{P_n(p,q)} + \frac{Q_3(p,q)}{P_n(p,q)^3} + \frac{Q_5(p,q)}{P_n(p,q)^5} + O\left(\frac{1}{P_n(p,q)^7}\right)$$

where $P_n(p,q)$ is as defined above and

$$\begin{aligned}
Q_1(p,q) &= \frac{p+3q}{8pq(q-p)},\\
Q_3(p,q) &= \frac{25p^4 - 31p^3q - 36p^2q^2 + 9pq^3 - 63q^4}{384(q-p)^2q^3p^3},\\
Q_5(p,q) &= \frac{3219p^7 - 6938p^6q + 2279p^5q^2 + 2040p^4q^3 + 360p^3q^4 + 4797p^2q^5 - 7614pq^6 + 5697q^7}{15360p^5q^5(q-p)^3}.
\end{aligned}$$

If on the other hand $q < p$ then from (B.2)

$$x\left[1 + \frac{\alpha_1(px) - \alpha_0(qx)}{(q-p)x}\right] = \bar{P}_n(p,q)$$

where

$$\bar{P}_n(p,q) = \frac{\pi(\frac{1}{2} - n)}{q-p}$$

and n is now a strictly positive integer. Notice that $\bar{P}_n(p,q) = P_n(q,p)$ and the remaining terms in the expansion are obtained in the same way as for the case $q > p$.

C Derivation of (3.16) and (3.17)

Here approximations for eigenvalues λ_n and μ_n in equations (3.11) are derived for the case of large R. Attention is focussed on the smallest eigenvalues since they exert the greatest influence on the solution (3.10). The following Bessel function expansions, valid as $x \to 0$, will be used

$$\begin{aligned}
J_0(x) &= 1 - \frac{x^2}{4} + O(x^4),\\
Y_0(x) &= \frac{2}{\pi}\ln\left(\frac{xe^\gamma}{2}\right) - \frac{x^2}{2\pi}\left[\ln\left(\frac{xe^\gamma}{2}\right) - 1\right] + O(x^4\ln(x)),\\
J_1(x) &= \frac{x}{2} - \frac{x^3}{16} + \frac{x^5}{384} + O(x^7),\\
Y_1(x) &= -\frac{2}{\pi x} + \frac{x}{\pi}\left[\ln\left(\frac{xe^\gamma}{2}\right) - \frac{1}{2}\right] - \frac{x^3}{8\pi}\left[\ln\left(\frac{xe^\gamma}{2}\right) - \frac{5}{4}\right] + \frac{x^5}{192\pi}\left[\ln\left(\frac{xe^\gamma}{2}\right) - \frac{5}{3}\right] + O(x^7\ln(x)),
\end{aligned} \tag{C.1}$$

where γ denotes Euler's constant.

C.1 Derivation of (3.16): approximation for small λ_n

We recall that λ_n satisfies

$$J_1\left(\sqrt{\lambda_n}\right) Y_0\left(R\sqrt{\lambda_n}\right) = Y_1\left(\sqrt{\lambda_n}\right) J_0\left(R\sqrt{\lambda_n}\right). \tag{C.2}$$

As $R \to \infty$, by numerically solving equation (C.2), we find that $\lambda_n \to 0$. First we expand the two functions of only $\sqrt{\lambda_n}$ using the expansions for $J_1(x)$ and $Y_1(x)$ in (C.1). Then multiplying by $2\pi\sqrt{\lambda_n}$ yields

$$\left(\pi\lambda_n + O({\lambda_n}^2)\right) Y_0\left(R\sqrt{\lambda_n}\right) = \left(-4 + O(\lambda_n \ln(\lambda_n))\right) J_0\left(R\sqrt{\lambda_n}\right). \tag{C.3}$$

By numerically solving equation (C.2) we find that $R\sqrt{\lambda_n}$ tends to a constant as $R \to \infty$, so we seek an expansion in the form

$$R\sqrt{\lambda_n} = \zeta_n + \epsilon. \tag{C.4}$$

We use the Taylor series expansions as $\epsilon \to 0$ and substituting into (C.3) yields

$$\begin{aligned}\left(\pi\frac{\zeta_n^2}{R^2} + O(\epsilon R^{-2}, R^{-4})\right) &\left(Y_0(\zeta_n) + \epsilon Y_0'(\zeta_n) + O(\epsilon^2)\right) \\ &= \left(-4 + O(R^{-2}\ln(R))\right)\left(J_0(\zeta_n) + \epsilon J_0'(\zeta_n) + O(\epsilon^2)\right).\end{aligned}$$

Notice that in the equation above, as $R \to \infty$ the left hand side tends to zero, but the right hand side tends to $-4J_0(\zeta_n)$. Thus we require

$$J_0(\zeta_n) = 0. \tag{C.5}$$

Hence the ζ_n's in (C.4) are the n^{th} roots of J_0. Using this and keeping the leading order terms yields

$$\frac{\pi\zeta_n^2}{F^2} Y_0(\zeta_n) + O(\epsilon R^{-2}, R^{-4}) = -4\epsilon J_0'(\zeta_n) + O(\epsilon R^{-2}\ln(R), \epsilon^2).$$

Thus, to leading order,

$$\epsilon = -\frac{\pi\zeta_n^2 Y_0(\zeta_n)}{4R^2 J_0'(\zeta_n)} + O(R^{-4}\ln(R)).$$

Hence, from (C.4) it follows that

$$\sqrt{\lambda_n} = \frac{\zeta_n}{R} - \frac{\pi\zeta_n^2 Y_0(\zeta_n)}{4R^3 J_0'(\zeta_n)} + O(R^{-5}\ln(R)), \tag{C.6}$$

which is valid for $\sqrt{\lambda_n} \ll 1$, i.e. $\zeta_n \ll R$.

C.2 Approximation for small μ_n, $n \geq 2$

Recall that the eigenvalue μ_n satisfies

$$J_1\left(R\sqrt{\mu_n}\right) Y_0\left(\sqrt{\mu_n}\right) = Y_1\left(R\sqrt{\mu_n}\right) J_0\left(\sqrt{\mu_n}\right). \tag{C.7}$$

As $R \to \infty$, by numerically solving equation (C.7), we find that $\mu_n \to 0$. First, we expand the two functions of only $\sqrt{\mu_n}$ using the series for $J_0(x)$ and $Y_0(x)$ in equation (C.1) so that equation (C.7) becomes

$$J_1(R\sqrt{\mu_n})\left(\frac{2}{\pi}\ln\left(\frac{\sqrt{\mu_n}e^{\gamma}}{2}\right) + O(\mu_n \ln(\mu_n))\right) = Y_1(R\sqrt{\mu_n})(1 + O(\mu_n)). \tag{C.8}$$

By numerically solving equation (C.7) we find that $R\sqrt{\mu_n}$ tends to a constant as $R \to \infty$, so we seek an expansion in the form

$$R\sqrt{\mu_n} = \theta_n + \delta. \tag{C.9}$$

A Taylor series expansion as $\delta \to 0$ is constructed from equation (C.8) resulting in

$$\begin{aligned}\left(J_1(\theta_n) + \delta J_1'(\theta_n) + O(\delta^2)\right)\left(\frac{2}{\pi}\ln\left(\frac{(\theta_n+\delta)e^{\gamma}}{2R}\right) + O(R^{-2}\ln(R))\right) \\ = \left(Y_1(\theta_n) + \delta Y_1'(\theta_n) + O(\delta^2)\right)\left(1 + O\left(R^{-2}\right)\right).\end{aligned}$$

We notice that in the equation above, as $R \to \infty$ the right hand side remains finite, but the left hand side tends to infinity like $-2\ln(R)J_1(\theta_n)/\pi$. Thus, we require

$$J_1(\theta_n) = 0. \tag{C.10}$$

Hence the θ_n's in (C.9) are the n^{th} roots of J_1 and note that $\theta_1 = 0$ is the first solution. Before collecting leading order terms, notice that the approach fails around θ_1 since $Y_1(0)$ is undefined and hence an alternative approach is required for the calculation of μ_1 (see subsection C.3).

Provided $n \geq 2$, keeping the leading order terms yields

$$-\delta J_1'(\theta_n)\frac{2}{\pi}\ln(R) = Y_1(\theta_n) + O\left(\delta, R^{-2}, R^{-2}\ln(R)\delta\right).$$

Thus, to leading order and provided $1 \ll \ln(R)$, i.e. $e \ll R$,

$$\delta = -\frac{\pi Y_1(\theta_n)}{2J_1'(\theta_n)\ln(R)} + O\left(\frac{1}{\ln(R)^2}, \frac{R^{-2}}{\ln(R)}\right).$$

Hence from (C.9) we have

$$\sqrt{\mu_n} = \frac{\theta_n}{R} - \frac{\pi Y_1(\theta_n)}{2R\ln(R)J_1'(\theta_n)} + O\left(\frac{R^{-1}}{\ln(R)^2}, \frac{R^{-3}}{\ln(R)}\right), \tag{C.11}$$

which is valid for $\sqrt{\mu_n} \ll 1$, i.e. $\theta_n \ll R$ (and the condition $e \ll R$ is ensured since $e < \theta_2$).

C.3 Derivation of (3.17): approximation for small μ_1

The above approach failed to calculate μ_1 because $Y_1(0)$ is not defined and hence an alternative approach, utilizing a different expansion, is described here. Recall μ_1 satisfies

$$J_1(R\sqrt{\mu_1})Y_0(\sqrt{\mu_1}) = Y_1(R\sqrt{\mu_1})J_0(\sqrt{\mu_1}). \tag{C.12}$$

As $R \to \infty$, by numerically solving equation (C.12), we find that $R\sqrt{\mu_1} \to 0$. By substituting all the expansions in equation (C.1) into equation (C.12) it follows that

$$\begin{aligned}\left(\frac{R\sqrt{\mu_1}}{2} - \frac{R^3\mu_1^{\frac{3}{2}}}{16} + \frac{R^5\mu_1^{\frac{5}{2}}}{384} + O(R^7\mu_1^{\frac{7}{2}})\right)\left(\frac{2}{\pi}\ln\left(\frac{\sqrt{\mu_1}e^\gamma}{2}\right) + O(\mu_1\ln(\mu_1))\right)\\ = (1+O(\mu_1)) \times \left(-\frac{2}{\pi R\sqrt{\mu_1}} + \frac{R\sqrt{\mu_1}}{\pi}\left[\ln\left(\frac{R\sqrt{\mu_1}e^\gamma}{2}\right) - \frac{1}{2}\right]\right.\\ \left. -\frac{R^3\mu_1^{\frac{3}{2}}}{8\pi}\left[\ln\left(\frac{R\sqrt{\mu_1}e^\gamma}{2}\right) - \frac{5}{4}\right] + \frac{R^5\mu_1^{\frac{5}{2}}}{192\pi}\left[\ln\left(\frac{R\sqrt{\mu_1}e^\gamma}{2}\right) - \frac{5}{3}\right] + O(R^7\mu_1^{\frac{7}{2}}\ln(R\sqrt{\mu_1}))\right).\end{aligned}$$

Multiplying by $2\pi R\sqrt{\mu_1}$ and cancelling out terms reduces this expression to

$$0 = -4 + R^2\mu_1\left[2\ln(R) - 1\right] - \frac{R^4\mu_1^2}{4}\left[\ln(R) - \frac{5}{4}\right] + \frac{R^6\mu_1^3}{96}\left[\ln(R) - \frac{5}{3}\right] + O(\mu_1, R^8\mu_1^4\ln(R\sqrt{\mu_1})). \tag{C.13}$$

Next, motivated by the presence of $\ln(R)$ and the powers of μ_1 in the above, we suppose that μ_1 can be expanded in the form

$$\mu_1 = \frac{1}{R^2\ln(R)}\left[a + \frac{b}{\ln(R)} + \frac{c}{\ln(R)^2} + O\left(\frac{1}{\ln(R)^3}\right)\right] \tag{C.14}$$

where a, b and c are constants to be determined. By substituting equation (C.14) into equation (C.13) and retaining leading order terms yields

$$\begin{aligned}O\left(\frac{1}{R^2\ln(R)}, \frac{\ln(\ln(R))}{\ln(R)^3}\right) = -4 + 2a + \frac{2b}{\ln(R)} + \frac{2c}{\ln(R)^2} - \frac{a}{\ln(R)} - \frac{b}{\ln(R)^2}\\ - \frac{a^2}{4\ln(R)} - \frac{ab}{2\ln(R)^2} + \frac{5a^2}{16\ln(R)^2} + \frac{a^3}{96\ln(R)^2}.\end{aligned}$$

Finally, by equating the coefficients of the powers of $\ln(R)$, values for a, b and c can be determined and hence

$$\mu_1 = \frac{1}{R^2\ln(R)}\left[2 + \frac{3}{2\ln(R)} + \frac{5}{6\ln(R)^2} + O\left(\frac{1}{\ln(R)^3}\right)\right], \tag{C.15}$$

which is valid for $e \ll R$.